Tungsten (2023) 5:371–390
https://doi.org/10.1007/s42864-023-00202-8

Tungsten
www.springer.com/42864

REVIEW PAPER

# Recent progress of $W_{18}O_{49}$ nanowires for energy conversion and storage

Nan-Fu Yan[1] · Hong-Min Cui[1] · Jin-Song Shi[1] · Sheng-Yong You[1] · Sheng Liu[2]

Received: 17 October 2022 / Revised: 24 November 2022 / Accepted: 29 November 2022 / Published online: 21 January 2023
© The Nonferrous Metals Society of China 2023

## Abstract

$W_{18}O_{49}$ nanowires ($W_{18}O_{49}$ NWs) with unique one-dimension structures and excellent electron/ions transport properties have attracted increasing attention in academia and industry because of their potential applications in many energy-related devices. In the past decades, many research articles related to $W_{18}O_{49}$ have been published, but there are insufficient review articles focusing on $W_{18}O_{49}$ NWs. In this review, we present the crystal structure of $W_{18}O_{49}$ and briefly introduce the synthesis methods and growth mechanism of $W_{18}O_{49}$ NWs. Moreover, their applications in energy conversion and storage devices are summarized. Finally, the current challenges and opportunities for applying $W_{18}O_{49}$ NWs are provided. We hope this review can promote the development of $W_{18}O_{49}$ NWs in energy conversion, storage, and other promising applications.

**Keywords** $W_{18}O_{49}$ nanowires · Photovoltaic · Rechargeable batteries · Capacitors · Fuel production

## 1 Introduction

To achieve the goals of carbon peak and carbon neutrality, countries around the world need to deal with the challenge of the large and still growing base of $CO_2$ emission [1, 2]. The world is actively releasing implementation plans to achieve peak $CO_2$ emissions in key areas and sectors as well as a series of supporting measures to meet the goal of carbon peak and neutralization [3–5]. Among them, developing and utilizing more renewable energy from natural resources is considered the most effective solution. However, large-scale deployment of natural resources still has many inherent drawbacks, such as the intermittency of solar and wind [6–8]. Fortunately, there are many valuable technologies to overcome the shortage of clean energy from natural resources, such as rechargeable batteries, capacitors, solar cells, and fuel cells. As is known to all, the excellent performance of all the above devices is intimately and largely dependent on the remarkable properties of their materials. Thus, developing highly efficient materials to construct highly efficient devices is essential. Although these technologies harness clean energy from natural resources, large-scale clean energy utilization is still a long way to go. Therefore, more intensive investigations to explore new high-performance materials are urgently desired to construct highly efficient devices for using large-scale natural resources.

Non-stoichiometric tungsten oxides ($WO_{3-x}$) have attracted increasing interest due to their unique properties [9–13]. It is widely known that $W_{18}O_{49}$ is an important material in the family of $WO_{3-x}$, which has been extensively investigated owing to its earth abundance, highly tuneable composition, and high chemical stability. Especially, $W_{18}O_{49}$ nanowires ($W_{18}O_{49}$ NWs) are unique and versatile because they inherit all typical features of $W_{18}O_{49}$ bulk and also display a high aspect ratio, which is a benefit for photogenerated carriers to transfer along the axial direction. Meanwhile, the relatively large specific surface area and chemical stability of $W_{18}O_{49}$ NWs also make it an ideal building block for assembling various heterostructures, which allow $W_{18}O_{49}$ NWs materials applicable in smart windows [14, 15], electrochromic devices [16–18], photothermal therapy [19, 20], gases sensors [21–23], photodetector [24], photocatalysis

✉ Nan-Fu Yan
nfyan@mail.nankai.edu.cn

✉ Sheng Liu
shengliu@nankai.edu.cn

[1] Institute of Applied Chemistry, Jiangxi Academy of Sciences, Nanchang 330096, China

[2] Institute of New Energy Material Chemistry, School of Materials Science and Engineering, Renewable Energy Conversion and Storage Center, Nankai University, Tianjin 300350, China

[25–27], and so on. Recently, $W_{18}O_{49}$ NWs have been extensively studied in the energy conversion and storage area, including photovoltaic, fuel cells, rechargeable batteries, and capacitors [11]. Therefore, one-dimensional (1D) $W_{18}O_{49}$ NWs have been considered a substantially promising target material due to their unique anisotropic morphologies and abundant structure tuning capabilities. Since the pioneering work of preparing $W_{18}O_{49}$ NWs with diameters in tens of nanometers was reported, the research works on $W_{18}O_{49}$ NWs have achieved fast developments and brought substantial opportunities.

To date, there has been just one review that focuses on $W_{18}O_{49}$ for photocatalytic applications [28]. No review paper has focused on the applications of 1D $W_{18}O_{49}$ NWs for energy conversion and storage. In this review, we first provided a detailed discussion of the crystal structure of $W_{18}O_{49}$ and a brief introduction to the synthesis and growth mechanism of $W_{18}O_{49}$ NWs. Then the applications of $W_{18}O_{49}$ NWs in energy conversion applications, including photovoltaic, fuel cells, and fuel production, are summarized. Afterward, we reviewed the applications of $W_{18}O_{49}$ NWs in the electrochemical energy storage field, such as rechargeable batteries, capacitors, and electrochromic energy storage systems. Finally, the main future research directions on $W_{18}O_{49}$ NWs and energy-related applications were proposed. We hope this review will inspire more research and stimulate extensive future studies in this rapidly growing research field.

## 2 Crystal structure and synthesis of $W_{18}O_{49}$ NWs

### 2.1 Crystal structure of $W_{18}O_{49}$

$W_{18}O_{49}$ is a typical non-stoichiometric tungsten oxide, which can be refined in a pure form as a monoclinic structure type (P2/m) [29–31]. The crystal structure of $W_{18}O_{49}$ has been described in detail in previous literature [29, 30, 32], as shown in Fig. 1a, b. The crystal structure of $W_{18}O_{49}$ contains distorted $WO_6$ octahedra, which links together by sharing corner. It is well known that the crystal structure of $W_{18}O_{49}$ has multiple valency tungsten ions and includes a considerable amount of oxygen deficiency [33–35]. To compensate for the oxygen deficiency in the crystal structure of $W_{18}O_{49}$, a part of edge sharing of the $WO_6$ octahedra occurs in the existing corner sharing [33]. The possibilities of sharing modes between the $WO_6$ octahedra building blocks are illustrated in Fig. 1c. Owing to the well-ordered corner/edge-sharing $WO_6$ framework, the lattice network forms an open structure consisting of trigonal, quadrangular, and hexagonal tunnels [33]. As shown in Fig. 1d, it is clear that $W_{18}O_{49}$ has a large unit cell containing pore-like tunnels. These innate channels in the $W_{18}O_{49}$ structure can provide accommodation and diffusion pathways for cations [36, 37]. Specifically, $W_{18}O_{49}$ has strong anisotropic growth behavior along the [010] direction, which makes $W_{18}O_{49}$ easy to form 1D structure, such as nanofibers, nanowires [38, 39], and nanorods [40, 41]. Anisotropic growth-induced $W_{18}O_{49}$ NWs possess

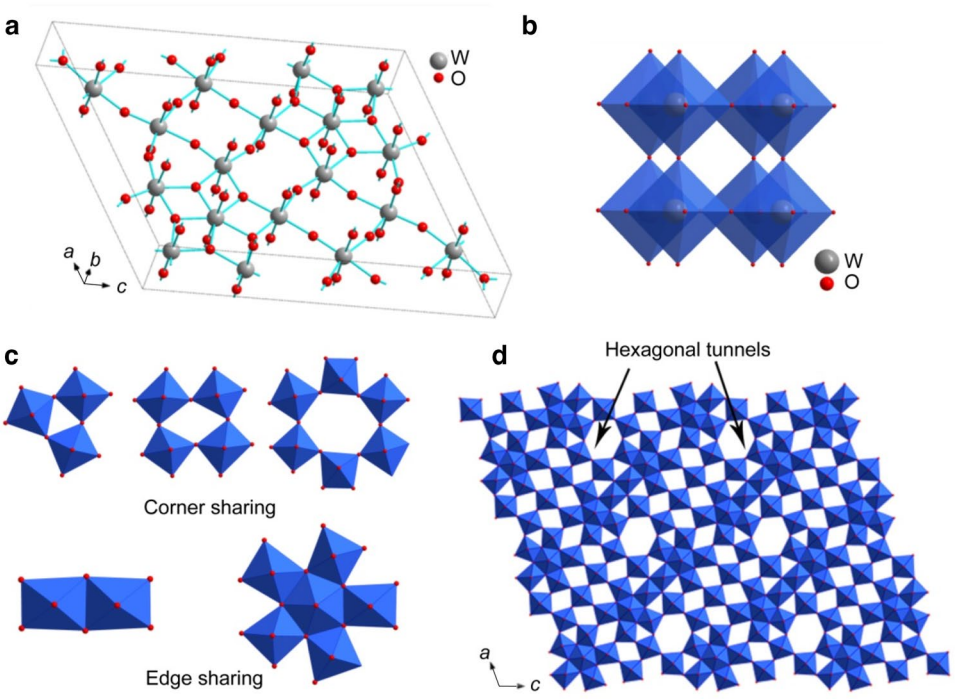


**Fig. 1** **a** Unit cells of $W_{18}O_{49}$. **b** Atomic structural model of monoclinic $W_{18}O_{49}$ showing $WO_6$ octahedra. Reproduced with permission from Ref. [30]. Copyright 1981. Elsevier. **c** Possibilities of sharing modes between building blocks. **d** The continuous structure of $W_{18}O_{49}$ with hexagonal tunnels. Reproduced with permission from Ref. [33]. Copyright 2021, Springer

a larger surface-to-volume ratio and high aspect ratio than the bulk $W_{18}O_{49}$. Therefore, these unique structural characteristics of the $W_{18}O_{49}$ NWs provide advantages in several applications.

### 2.2 Synthesis and growth mechanism of $W_{18}O_{49}$ NWs

Substantial previous research results have confirmed that the physical and chemical properties of synthetic nanowire materials can be significantly improved or radically tailored when their sizes are reduced to the nanometer regime due to effects such as a high surface-to-volume ratio and quantum confinement. Therefore, the design and fabrication of high-quality nanowires are critical to exploring $W_{18}O_{49}$ NWs-based high-performance energy conversion and storage devices. Since the first synthesis of $W_{18}O_{49}$ NWs by infrared (IR) irradiation thermal evaporation approach, various methods have been successfully developed to synthesize $W_{18}O_{49}$ NWs, including solvothermal [42–45], thermal evaporation [46–48], hydrothermal [49–51], chemical vapor deposition [52–54], template-assisted [55] and microwave-assisted method [56], electron beam irradiation [57, 58], and so on. With the unremitting efforts of scientists, significant progress has been achieved in controlling the morphology, size, composition, and doping of $W_{18}O_{49}$ NWs. Nonetheless, the large-scale synthesis of $W_{18}O_{49}$ NWs with high quality using more environmentally friendly and low-cost methods remains a great challenge.

Generally speaking, different morphologies would result in different performances [59]. Therefore, it is vital to clarify the growth mechanism of $W_{18}O_{49}$ NWs for extending the applications. Although several methods have been reported for successfully preparing $W_{18}O_{49}$ NWs, relatively few articles have focused on the growth mechanism of the $W_{18}O_{49}$ NWs. This section will present the progress of the growth mechanisms of $W_{18}O_{49}$ NWs prepared by the thermal annealing and solvothermal methods. Thermal annealing methods are quick and modest for preparing $W_{18}O_{49}$ NWs. Currently, three kinds of growth mechanisms of $W_{18}O_{49}$ NWs using thermal annealing methods were reported, including $WO_2$ intermediate layer growth mechanism, vapor–solid mechanism (V–S), and solid-state (S-S) growth mechanism. The $WO_2$ intermediate layer growth mechanism may be divided into three steps, which are illustrated in Fig. 2a [60, 61]. First, the W particle surfaces were first oxidized into the $WO_2$ layer. Secondly, the W–O–W chains are broken when the water vapor reacts with the surface of the $WO_2$ layers, and then the $W_{18}O_{49}$ crystal nuclei form and grow along the [010] direction. Thirdly, as the oxidation reaction progresses, the W particles are exhausted while the long $W_{18}O_{49}$ NWs are obtained. The V–S may be divided into four steps, as summarized in Fig. 2b [62–64]: (1) a thin $WO_x$ layer was formed on the surface of the W film; (2) $WO_x{\cdot}nH_2O$ was generated on the outer $WO_x$ surface; (3) $WO_x{\cdot}nH_2O$ starts to decompose when the vapor pressure of volatile $WO_x{\cdot}nH_2O$ increases owing to the continuous oxidation of the tungsten film, and then the $W_{18}O_{49}$ crystal nuclei form and grow steadily while the $WO_x{\cdot}nH_2O$ decomposes; (4) as the reaction progresses, the long $W_{18}O_{49}$ nanowires are obtained. The S-S growth mechanism is illustrated in Fig. 2c [65]. First, $H_2O$ reacts with W to form $WO_3$ and $H_2$. Secondly, the $WO_3$ is reduced by $H_2$ to form $W_{18}O_{49}$. Thirdly, as the reactions (1) and (2) are repeated, long $W_{18}O_{49}$ NWs are obtained. Meanwhile, solvothermal is another widely used method for preparing $W_{18}O_{49}$ NWs. Although solvothermal methods have been commonly reported in the literature, relatively few studies have explored the mechanism. A possible growth mechanism of $W_{18}O_{49}$ NWs using the solvothermal method is shown in Fig. 2d [44]. It can be simulated as follows: (1) $H_2O$ between the $H_2WO_4$ layers is exchanged by alcohol or the intercalation of alcohol; (2) $H_2WO_4$ reacts with oleylamine to obtain tungstate oleylamine salt; (3) nucleation of $W_{18}O_{49}$ occurs and grows steadily while the tungstate oleylamine salt starts decomposing; (4) as the reaction progresses, $W_{18}O_{49}$ NWs with different diameters and lengths are obtained. Although numerous experiments have been conducted to understand the growth mechanism of $W_{18}O_{49}$ NWs during the last decade, the details of the growth mechanisms that occur during the synthesis of $W_{18}O_{49}$ NWs are still elusive. There is no doubt that more studies are needed to further clarify the underlying mechanism. Moreover, a precise and rapid growth mechanism is urgently desired to guide the large-scale synthesis of $W_{18}O_{49}$ NWs with controllable diameters and lengths.

## 3 $W_{18}O_{49}$ NWs for energy conversion

### 3.1 $W_{18}O_{49}$ NWs for photovoltaic applications

Large-scale utilization of solar energy and technologies is the final solution to address the excess emissions of $CO_2$. Photovoltaics (PV) or solar cells have been considered the most efficient way to utilize solar energy on a large scale [66–68]. Exploring and investigating new materials and technology is the intrinsic driving force for the gradual progress of PV [69, 70]. Over the past decades, scientists have struggled to search for efficient and low-cost materials to construct high-performance PV [71–74]. Pt is a well-known counter electrode catalyst for redox mediators in dye-sensitized solar cells (DSSCs) [75]. However, its scarcity and high cost limit its practical application [76–78]. Unfortunately, Pt is not always the best catalyst for all redox mediators. For instance, the catalytic effect of Pt catalysts is not very good when redox mediators are organic disulfide and

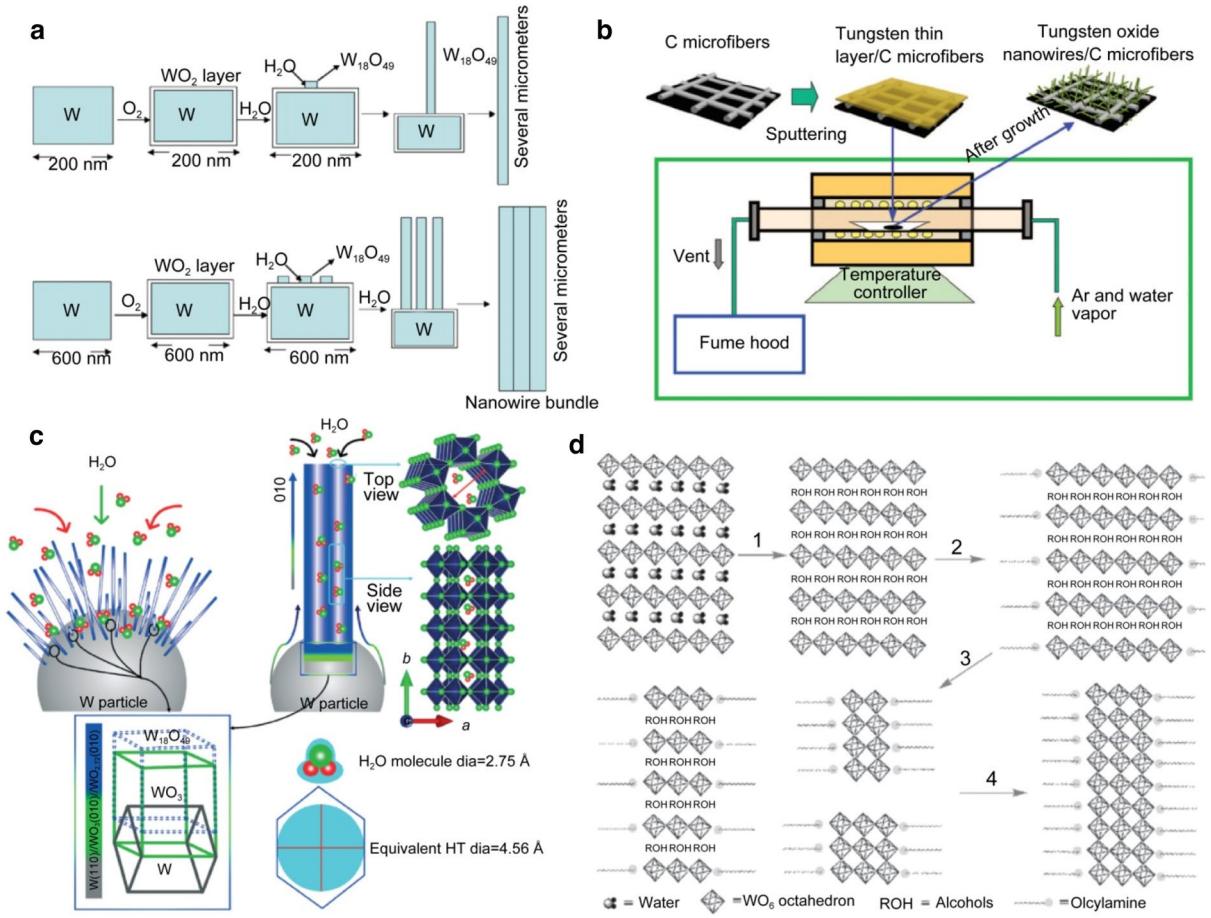


**Fig. 2** Several typical growth mechanisms of $W_{18}O_{49}$ NWs. **a** $WO_2$ intermediate layer growth mechanism, reproduced with permission from Ref. [61]. Copyright 2008. Elsevier. **b** V–S mechanism, reproduced with permission from Ref. [64]. Copyright 2009, American Chemical Society. **c** S-S growth mechanism, reproduced with permission from Ref. [65]. Copyright 2021. The Royal Society of Chemistry. **d** $W_{18}O_{49}$ NWs growth mechanism by solvothermal method. Reproduced with permission from Ref. [44]. Copyright 2014, Wiley-VCH

alkali metal polysulfide [79–81]. Therefore, developing a low-cost, high-performance electrocatalyst to take the place of Pt is highly desirable in DSSCs.

1D $W_{18}O_{49}$ NWs have massive surface oxygen vacancies and high charge carrier density, which make $W_{18}O_{49}$ NWs very suitable as catalytic electrodes in DSSCs. Currently, $W_{18}O_{49}$ NWs with high surface oxygen vacancy (SOV) content were successfully synthesized and used as the catalyst for electrocatalytic reduction of redox mediators ($I^-/I_3^-$) in DSSCs [82]. The scanning electron microscope (SEM) images of the $W_{18}O_{49}$ NWs before and after the SOV filling treatment are shown in Fig. 3a, b. It was found that there was a significant reduction in photoelectric conversion efficiencies (PCE) as the filling of SOVs time of the $W_{18}O_{49}$ NWs increased. It is shown in Fig. 3c that $W_{18}O_{49}$ NWs-based DSSCs achieved PCE of 7.8% due to the high SOVs content, which is close to that of Pt-based DSSCs. It was indicated that iodide reduction reaction activity was notably dependent on the SOVs of $W_{18}O_{49}$ NWs catalyst, which would serve as critical catalytic sites. The mechanism by which SOVs of $W_{18}O_{49}$ NWs regulate iodide reduction reactions and maintain the crystal phase and morphology of NWs was identified, as illustrated in Fig. 3d. It was confirmed that these findings would clarify the fundamental features of SOVs on metal oxides and contribute to the rational design of efficient catalysts and supports. Besides, the $W_{18}O_{49}$ NWs–reduced graphene oxide (rGO) composite was also prepared and applied in DSSCs. The first principles calculations of the adsorption energy between $I_3^-$ molecule and $W_{18}O_{49}$ NWs demonstrated that $W_{18}O_{49}$ NWs had good catalytic activity. Cyclic voltammetry (CV), electrochemical impedance spectroscopy, and Tafel polarization tests also further confirmed that the $W_{18}O_{49}$–rGO presented high electrocatalytic activity for reducing $I_3^-$ and low interface charge transfer impedance. Owing to the high electrocatalytic activity and low interface charge transfer impedance, the DSSCs based on

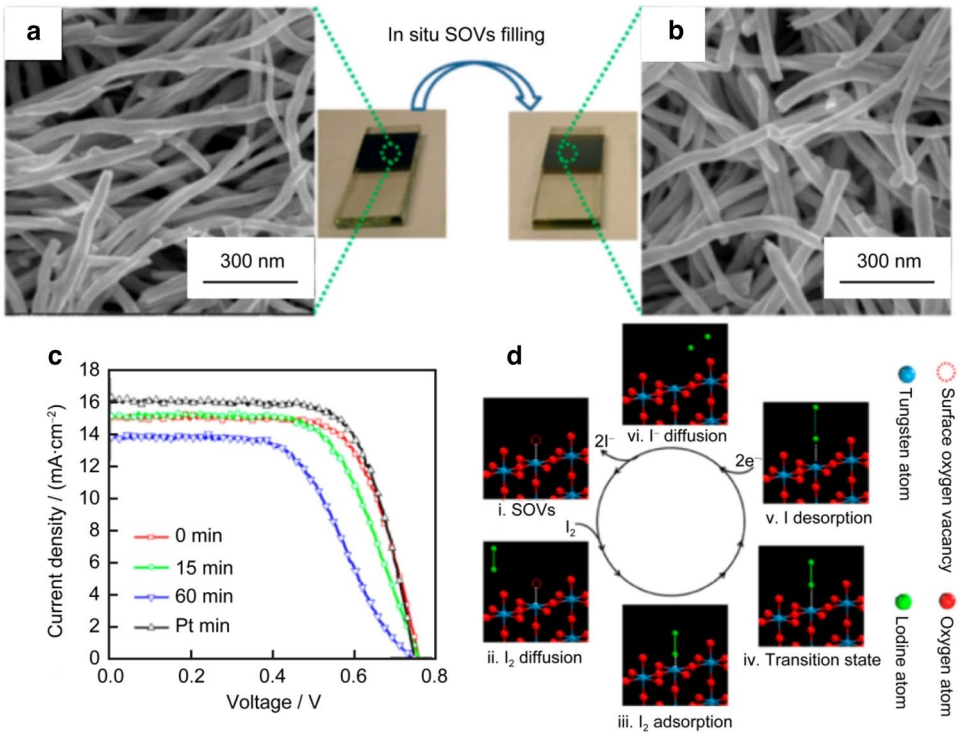


**Fig. 3** **a, b** SEM of the $W_{18}O_{49}$ with or without SOVs filling, **c** photocurrent density–voltage curves of DSSCs utilizing $I^-/I_3^-$ as the redox mediator, **d** schematic mechanism of SOVs as an important catalytic site for electrocatalysis. Reproduced with permission from Ref. [82]. Copyright 2014, American Chemical Society

$W_{18}O_{49}$–rGO achieved a PCE of 7.23%, which was comparable to the PCE of Pt-based DSSC (7.39%)[83]. Meanwhile, the mechanism on SOVs of $W_{18}O_{49}$ was also successfully verified in the cobalt complex and ferrocenium redox mediators [84]. It was revealed that the catalytic performance of $W_{18}O_{49}$ NWs for cobalt complex and ferrocenium redox mediators was also comparable to that of Pt. It was also found that the reduction reaction activity of the cobalt complex decreased slightly, whereas it increased slightly for ferrocenium after SOVs filling. In general, a clear relationship between the surface of electrocatalysts and the catalytic properties of different redox mediators will be helpful to the rational design of efficient catalysts in DSSCs. These works enriched the understanding of heterogeneous catalytic reactions on the surface of transition metal complexes for different redox mediators.

Moreover, $W_{18}O_{49}$ NWs exhibit excellent interfacial contact and excellent electrical conductivity caused by oxygen vacancies, which make them suitable as functional materials in organic solar cells (OSCs) and perovskite solar cells (PSCs). Specifically, $W_{18}O_{49}$ NWs film exhibit obviously improved ambient stability compared to poly(3,4-ethylenedioxythiophene)-poly (styrenesulfonate) (PEDOT:PSS) layer due to the inherently neutral and hydrophobic character of the $W_{18}O_{49}$ NWs. For instance, $W_{18}O_{49}$ NWs were successfully synthesized and used as an anode buffer layer in OSCs, which was confirmed as an alternative to conventional acidic PEDOT:PSS [85]. It was shown in Fig. 4a, b that the length of the as-prepared $W_{18}O_{49}$ was up to several micrometers and the diameter was below 30 nm. The energy level diagram of each material and the molecule structures of donors applied in fabricating OSCs are shown in Fig. 4c. When $W_{18}O_{49}$ NWs were used as the anode buffer layer in Fig. 4d–f, OSCs based on three typical polymer active layers PTB7:PC71BM, PTB7-Th:PC71BM, and PDBT-T1:PC71BM achieved higher PCEs of 8.23%, and 9.30%, and 9.09%, respectively. As a comparison, OSCs only obtained PCEs of 7.27%, 8.44% when PEDOT:PSS were used as the anode buffer layer. The results suggested that $W_{18}O_{49}$ NWs film was a promising candidate for organic solar cells' anode buffer layer materials. In addition, $W_{18}O_{49}$ NWs were also successfully applied in fabricating the hole transport layer for all-inorganic $CsPbBr_3$ PSCs [86]. It was revealed that $W_{18}O_{49}$ NWs with high work function promoted the hole extraction and reduced charge carrier recombination, resulting in a champion efficiency of 9.17% with a high Voc of 1.592 V for $CsPbBr_3$ PSCs. The profound advantages, good stability, and applicability for potential ease manufacturing processes make $W_{18}O_{49}$ NWs a good candidate for the hole transport layer in OSCs and PSCs. Meanwhile, there is still a lack of relevant research in the preparation of large-area solar cells using $W_{18}O_{49}$ NWs, which would be the direction for scientists to work on in the future.

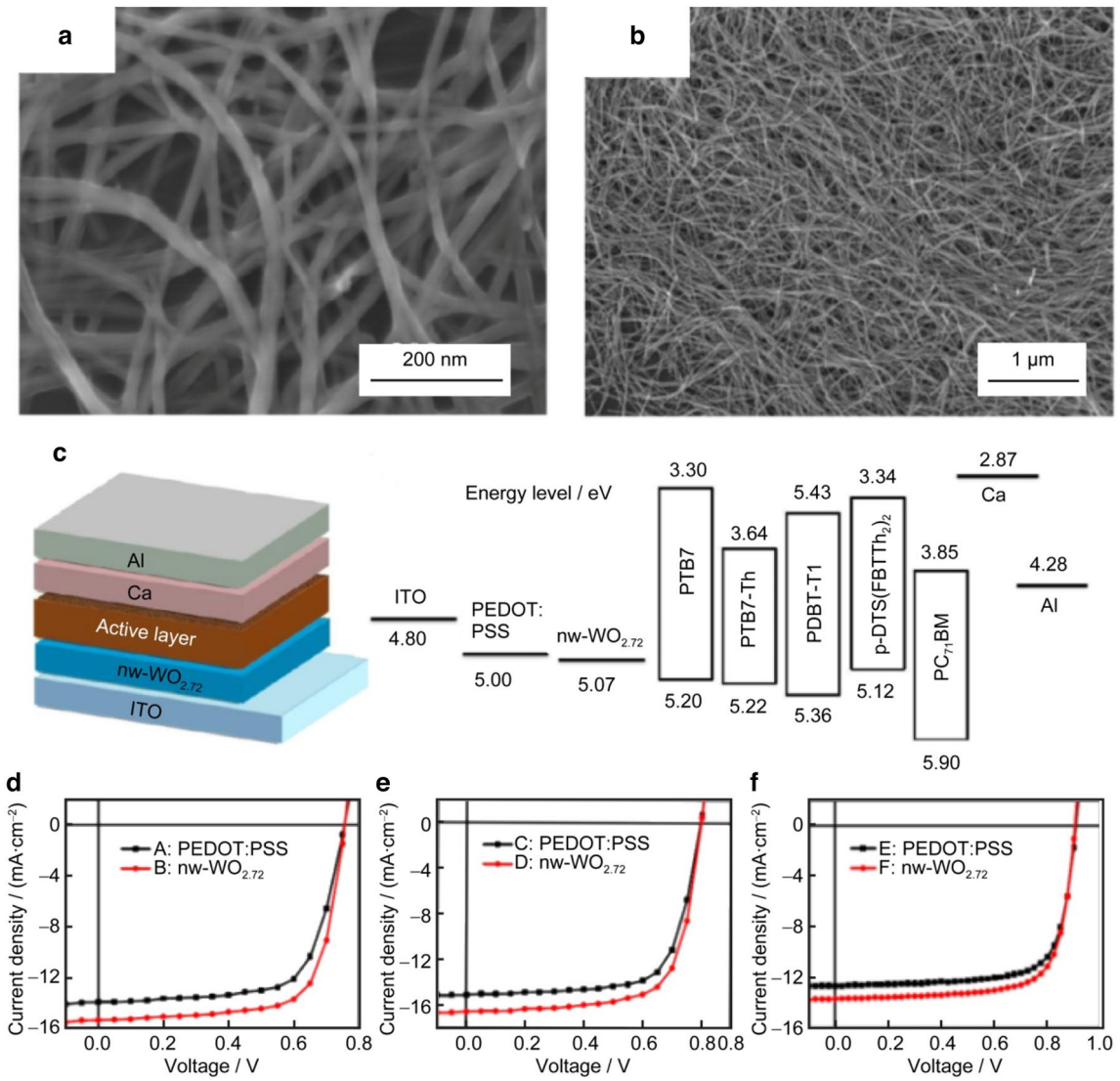


**Fig. 4** SEM images of the $W_{18}O_{49}$ with **a** high magnification and **b** low magnification. **c** Device architecture and energy levels of materials. J–V characteristics of OSCs based on the active layers of **d** PTB7:PC71BM, **e** PTB7-Th:PC71BM, **f** PDBT-T1:PC71BM. Reproduced with permission from Ref. [85]. Copyright 2017, American Chemical Society

### 3.2 $W_{18}O_{49}$ NWs for fuel cells

Three-dimensional structure (3D) can provide more reaction sites due to the higher spatial complexity. Thus, the 3D structural design strategy is a practical and versatile approach to improving the performance of materials. Therefore, the proper design of $W_{18}O_{49}$ NWs-based 3D electrodes could bring a promising path for fabricating novel oxygen reduction catalysts with high performance, low cost, and high CO tolerance for fuel cells. 3D structure Pt/$W_{18}O_{49}$ NWs/carbon paper electrodes were successfully designed and investigated as an oxygen reduction catalyst [87, 88]. Experimental results of the linear scan voltammogram showed that $W_{18}O_{49}$ NWs-based 3D electrodes presented higher electrocatalytic activity toward the oxygen reduction reaction than conventional Pt/C electrodes. Importantly, $W_{18}O_{49}$ NWs-based 3D electrodes also exhibited better CO tolerance. Based on the above catalyst design strategy, Pt/$W_{18}O_{49}$ NWs/carbon paper composite was prepared and successfully applied in proton exchange membrane fuel cells (PEMFCs) [87]. SEM images revealed that $W_{18}O_{49}$ NWs covered the carbon microfibers and formed a three-dimensional hierarchical electrode structure, as shown in Fig. 5a, b. Transmission electron microscope (TEM) images in Fig. 5c, d show that the $W_{18}O_{49}$ are very straight, with an average length of about 15 μm and diameters of 20–60 nm. As shown in Fig. 5e, the polarization curves revealed that PEMFCs based on Pt/$W_{18}O_{49}$ NWs/carbon paper achieved

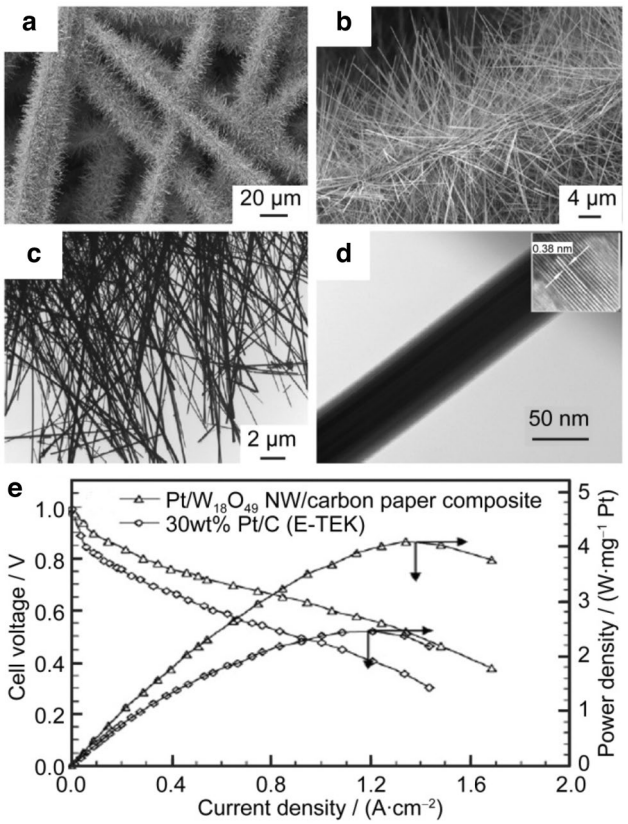


**Fig. 5** SEM and TEM images of $W_{18}O_{49}$ NWs grown on carbon microfibers of carbon paper. **a** Low magnification SEM. **b** High magnification SEM image. **c** Low magnification TEM image of $W_{18}O_{49}$ NWs. **d** TEM image of $W_{18}O_{49}$ NWs. **e** Polarization curves and power density curves in single-cell PEMFC. Reproduced with permission from Ref. [87]. Copyright 2009, Elsevier

a high current density of 1.04 $A{\cdot}cm^{-2}$. In contrast, PEMFCs based on Pt/C electrode only obtained a low current density of 0.56 $A{\cdot}cm^{-2}$ under the same conditions.

The combination of experimental and theoretical study is a very important approach to exploring new materials. The feasibility study of $W_{18}O_{49}$ NWs as catalyst supports for fuel cells was investigated in detail by theoretical calculation [89]. The theoretical calculation results revealed that $W_{18}O_{49}$ NWs with a 1.2 nm diameter showed potential as an oxygen reduction catalyst owing to their negative adsorption energy. Furthermore, the surface model of cobalt atom adsorbed onto the tungsten atoms on the $W_{18}O_{49}$ NWs (NWs–Co) surface revealed that it had high adsorption energy toward all molecules. Moreover, NWs–Co also could break the bond of oxygen in oxygen and hydrogen peroxide molecules to produce water as the main product. It was confirmed that the NWs–Co could oxidize carbon monoxide and methanol due to the high adsorption of NWs–Co toward these molecules. However, it can also bring mixed potential and thus reduce the performance of a single cell of direct methanol fuel cell (DMFC) when using it as a cathode catalyst. Fortunately, it was revealed that the adsorption of oxygen and hydrogen peroxide would be improved, and the adsorption of methanol and carbon monoxide would be reduced when the diameter of the $W_{18}O_{49}$ NWs was increased, or more cobalt atoms were added to the $W_{18}O_{49}$ NWs. Therefore, it is indicated that NW–Co had the potential to be used as catalyst support in the cathode for DMFC. Subsequently, the results of theoretical research were also proved successful in experiments [90, 91]. For instance, cobalt phthalocyanine-C/$W_{18}O_{49}$ NWs (CoPc-C/NWs) were prepared and successfully introduced as a non-platinum cathode catalyst for DMFCs [90]. It was revealed that the oxygen reduction reaction mechanism produced water as the main product when CoPc-C/NWs were used as catalysts, which had almost a 3.8-electron transfer number. It was demonstrated that the support of $W_{18}O_{49}$ NWs on CoPc enhanced the ORR activity. Single-cell DMFCs test showed that the power density was about 9.0 $mW{\cdot}cm^{-2}$ for CoPc-C/NWs. Importantly, CoPc-C/NWs also had excellent oxygen reduction activity in acidic media. Moreover, CoPc-C/NWs also did not react with methanol, which made it suitable as a feasible cathode catalyst for DMFC.

### 3.3 $W_{18}O_{49}$ NWs for fuel production

Direct conversion of $CO_2$ to fuels and value-added chemicals is a promising strategy to achieve the goals of carbon peak and carbon neutrality [92–94]. One of the main challenges associated with $CO_2$ reduction is exploring efficient catalytic materials for the activation of $CO_2$ [95, 96]. 1D $W_{18}O_{49}$ NWs have massive surface oxygen vacancies and high charge carrier density, which make $W_{18}O_{49}$ NWs very suitable as catalytic materials for $CO_2$ reduction.

$W_{18}O_{49}$ NWs with a 0.9 nm diameter were successfully synthesized and developed as an efficient photochemical catalyst for $CO_2$ reduction [31]. Photochemical reduction $CO_2$ experimental results showed that the average formation rate of methane was about 0.029 $mmol{\cdot}L^{-1}\ g^{-1}\ h^{-1}$ under irradiation with visible light. It was indicated from ultraviolet (UV)/visible (Vis) absorption spectroscopy and photoluminescence spectrum that the ultrathin $W_{18}O_{49}$ NWs consisted of a large number of oxygen vacancies, which was thought to be responsible for the high reactivity. The contrast test also confirmed that $CO_2$ reduction activity was notably dependent on $W_{18}O_{49}$ SOVs.

Meanwhile, surface modification engineering was used to improve the photoreduction ability of $W_{18}O_{49}$ NWs. $W_{18}O_{49}$ NWs decorated with isolated Co atoms were successfully synthesized and applied as an efficient catalyst for $CO_2$ photoreduction [97]. All experimental results and Density functional theory calculations confirmed that the energy band configuration of $W_{18}O_{49}$ NWs was greatly modified

after the decoration of Co atoms, which should be fundamentally responsible for improving the redox capability of photoexcited electrons for $CO_2$ reduction. The photocatalytic $CO_2$ reduction performance revealed that CO and $H_2$ generation rates were 21.18 and 6.49 mmol·g$^{-1}$ h$^{-1}$ for the first hour when the optimized $W_{18}O_{49}$@Co hybrid was used as the catalyst. As a comparison, the CO and $H_2$ generation rates of $W_{18}O_{49}$ without Co were poor and nearly undetectable. Besides, element doping was employed to design the high-performance catalyst to overcome the shortcomings of fast electron–hole recombination, which would result in low efficiency in photocatalytic $CO_2$ reduction. Currently, $Cu^+$-doped $W_{18}O_{49}$ NWs were successfully synthesized and applied as an efficient catalyst for $CO_2$ photoreduction [98]. The morphology, structure and the energy dispersive X-ray spectroscopy (EDX) mapping of $Cu^+$ doped $W_{18}O_{49}$ NWs was presented in Fig. 6a–c. The SEM and TEM images showed that the $W_{18}O_{49}$ presented a wire-like morphology with 25–40 nm diameters. As shown in Fig. 6d–h, Cu, O, and W elements were uniformly distributed in each nanowire in terms of the selected area. It was revealed that the conduction edge of $W_{18}O_{49}$ changed to a more negative position, and the electron–hole recombination was also effectively inhibited after $Cu^+$ doping. Moreover, $Cu^+$-doped $W_{18}O_{49}$ NWs showed relatively poor hydrophilicity, which could reduce the active sites occupied by $H_2O$ molecules. All of these were beneficial for the occurrence of $CO_2$ photoreduction. As shown in Fig. 6i, the photocatalytic $CO_2$ reduction performance revealed that the $CH_4$ generation rates were approximately 0.67 μmol·g$^{-1}$ h$^{-1}$ using $W_{18}O_{49}$ nanowires with a $Cu^+$ doping amount of 2.5%, while generation rates of 0.16 μmol·g$^{-1}$ h$^{-1}$ were obtained when using pure $W_{18}O_{49}$ NWs. The best activity $Cu^+$ doped $W_{18}O_{49}$ sample was roughly 4.0 times higher than that of pure $W_{18}O_{49}$ NWs. Therefore, transition metal doping and surface modification engineering strategies would provide an alternative for designing high-performance catalysts to reduce $CO_2$ into fuels.

Moreover, $W_{18}O_{49}$ NWs were used to assemble unique nanostructures for $CO_2$ reduction. For instance, Au/$TiO_2$/$W_{18}O_{49}$ NWs plasmonic heterostructure photocatalyst was successfully designed and constructed to overcome

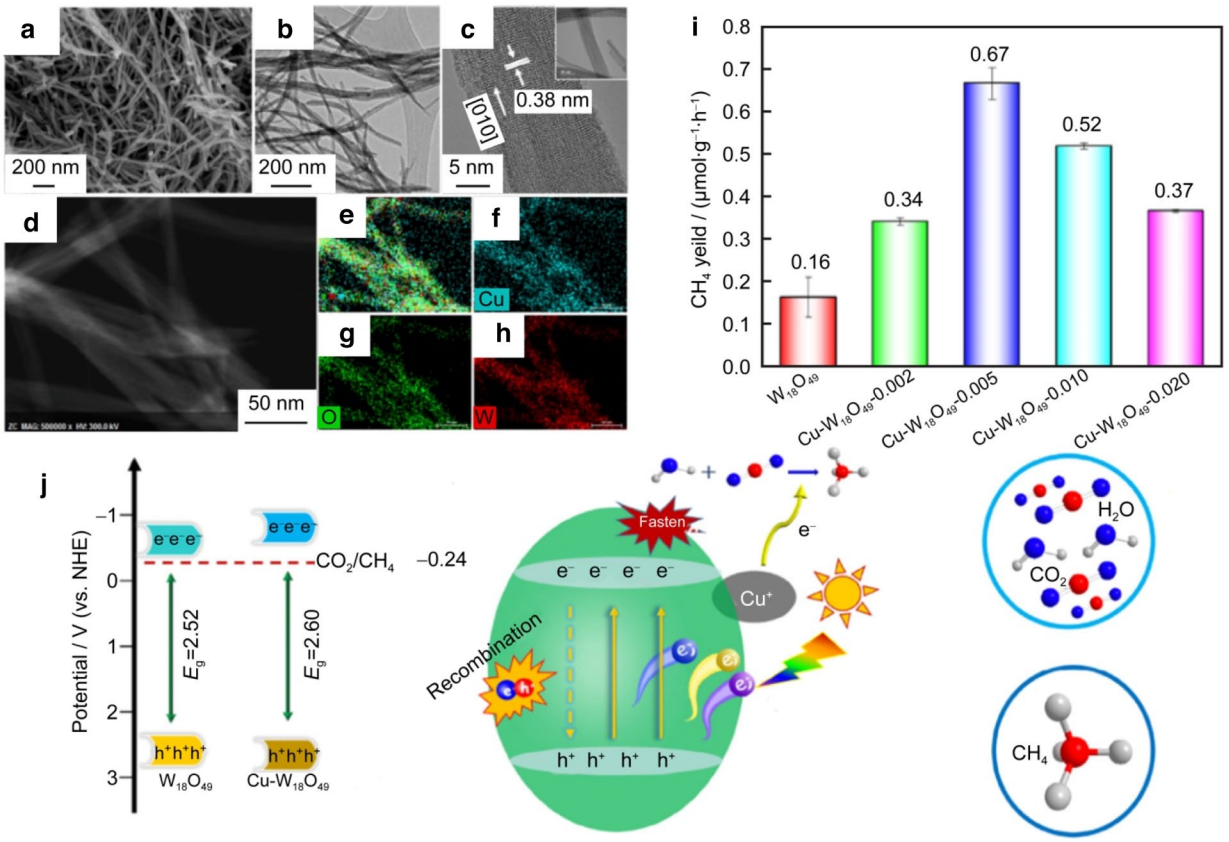


**Fig. 6** **a** SEM, **b** TEM, **c** high resolution transmission electron microscopy (HRTEM), **d** scanning transmission electron microscopy images, and **e–h** EDX mapping of the Cu–$W_{18}O_{49}$-0.005 sample. **i** Photoreduction of $CO_2$ into $CH_4$ upon $W_{18}O_{49}$ and Cu–$W_{18}O_{49}$-$x$ ($x$ = 0.002, 0.005, 0.01, and 0.02) products. **j** Schematic illustration of the electronic band structures of $W_{18}O_{49}$ nanowires and the Cu–$W_{18}O_{49}$-0.005 Sample and illustration of photocatalytic $CO_2$ reduction over $Cu^+$-doped $W_{18}O_{49}$ using $H_2O$ as reducing agent. Reproduced with permission from Ref. [98]. Copyright 2020, Elsevier

the disadvantages of poor efficiency and low selectivity for producing kinetically unfavorable hydrocarbons [99]. Owing to the interesting plasmon coupling between the Au and $W_{18}O_{49}$, the Au/$TiO_2$/$W_{18}O_{49}$ can strongly harvest incident light to generate high-energy hot electrons. Meanwhile, the Au/$TiO_2$/$W_{18}O_{49}$ can also adsorb intermediate products of CO and protons through the dual-heteroactive sites (Au–O–Ti and W–O–Ti) at their hetero-interface regions during the photocatalytic $CO_2$ reduction process. The theoretical and experimental results all confirmed that the well-designed Au/$TiO_2$/$W_{18}O_{49}$ plasmonic heterostructure could simultaneously confine high-energy hot electrons, protons, and CO during the photocatalytic $CO_2$ reduction process, which resulted in high photocatalytic activity of 35.55 μmol·$g^{-1}$ $h^{-1}$ and high selectivity of 93.3% for $CH_4$ production. Specifically, the CO generation rate was only 2.57 μmol·$g^{-1}$ $h^{-1}$. It was confirmed that the plasmonic active "hot spot"-confined photocatalysis strategy opened a new door for designing the new generation of plasmonic photocatalysts for high-efficiently converting $CO_2$ into valuable fuels.

As is known to all, hydrogen is considered a promising substitute for fossil fuels owing to its high energy density and cleanliness [100–103]. $W_{18}O_{49}$ NWs and their composites were also applied as an efficient photocatalyst for hydrogen generation. For instance, plasmonic $W_{18}O_{49}$ NWs were successfully used as a photocatalyst to accelerate hydrogen generation from ammonia borane [104]. Under visible light irradiation, $H_2$ evolution was 79.5 μmol in one hour with $W_{18}O_{49}$ NWs, compared to 14.8 μmol with commercial $WO_3$. However, the $H_2$ evolution efficiency of the single traditional semiconductor photocatalysts is still unsatisfactory. Therefore, the design of an ideal electrocatalyst for $H_2$ evolution is highly required to provide high energy efficiency. Recently, a significant amount of effort has also been devoted to improving the performance of $W_{18}O_{49}$ NWs via structure engineering or electron regulating [105–107]. Obviously, structure control has been proven to be an effective method to improve the active area and optimize the performance of $W_{18}O_{49}$ NWs, such as novel architecture and morphologies [105, 108–110]. Meanwhile, heteroatom doping has emerged as an easy and mild approach to generate active sites and regulate electronic structure to enhance the conductivity or catalytic activity of $W_{18}O_{49}$. For instance, Mo element doping has been reported to efficiently optimize the electronic structure of $W_{18}O_{49}$ NWs and thus significantly boost the hydrogen evolution reaction rate [111]. The above approaches that can fundamentally optimize the properties of materials have been proven to be effective strategies for designing high-performance $W_{18}O_{49}$ NWs-based catalysts.

Meanwhile, the rational construction of heterostructure plasmonic materials has also been proven to be an effective strategy for designing high-performance $W_{18}O_{49}$ NWs catalysts with a broad absorption range, long-term stability, high charge-separation efficiency and strong redox ability for high-efficiency $H_2$ generation. Currently, $W_{18}O_{49}$ NWs/$TiO_2$ branched heterostructure was successfully designed and constructed by the solvothermal method and applied as a model system to investigate the kinetics process and catalytic activity for $H_2$ generation under IR-light irradiation [112]. Figure 7a shows that the XRD patterns indicated the coexistence of characteristic diffraction peaks of monoclinic $W_{18}O_{49}$ and anatase $TiO_2$ in the $W_{18}O_{49}$ NWs/$TiO_2$. The SEM, TEM and EDX mapping images revealed that Ti was mainly distributed in the middle of the branched heterostructure and that W was dominant in the side region, which confirmed the structure of a $TiO_2$ nanofibers ($TiO_2$ NFs) backbone coated with $W_{18}O_{49}$ NWs branches, as illustrated in Fig. 7b–f. UV–Vis–IR absorption spectra in Fig. 7g suggested that the plasmonic $W_{18}O_{49}$ branches can strongly concentrate the incident light field with IR frequencies to generate energetic hot electrons surrounding the $W_{18}O_{49}$ NWs/$TiO_2$ interface. It was also revealed that the transfer of a plasmon-induced hot electron from the $W_{18}O_{49}$ branches to the $TiO_2$ backbones was completed within only about 200 fs, which is much faster than their relaxation process from the high-energy surface plasmon to the ground state (7–9 ps) in the $W_{18}O_{49}$ NWs. Thus, the generation and separation of a plasmonic hot electron in the $W_{18}O_{49}$/$TiO_2$ were greatly promoted due to the ultrafast kinetics feature, which led to a remarkably enhanced catalytic activity for $H_2$ generation compared to the activity of pure $W_{18}O_{49}$ NWs. As shown in Fig. 7h, the $H_2$ generation rate was about 0.014 μmol·$min^{-1}$ when $TiO_2$ NFs were used as a catalyst. It is indicated that $TiO_2$ NFs are almost inert for $H_2$ generation. The $H_2$ generation rate was about 0.50 μmol·$min^{-1}$ when $W_{18}O_{49}$ NWs were used as a catalyst. The good catalytic activity of the $W_{18}O_{49}$ NWs is ascribed to their abundant surface-active sites and strong localized surface plasmon resonance (LSPR) absorption in the IR region. More impressively, the $H_2$ generation rate was about 0.62 μmol·$min^{-1}$ when $W_{18}O_{49}$ NWs were assembled onto $TiO_2$ NFs. The $H_2$ generation rate based on $W_{18}O_{49}$/$TiO_2$ was almost about 1.24-fold compared with that of $W_{18}O_{49}$ NWs alone. It was indicated that the $TiO_2$ NFs could act as a sensitizer to further improve the plasmon-driven catalytic activity of the $W_{18}O_{49}$ NWs. The mechanism of IR-driven transfer of plasmon-induced hot electron in a nonmetallic heterostructure for enhanced $H_2$ generation was successfully verified, as illustrated in Fig. 7i. It is confirmed that the rational construction design is an ideal strategy for designing high-performance $W_{18}O_{49}$ NWs catalysts. Soon afterward, $Yb^{3+}$/$Er^{3+}$ doped $NaYF_4$/$W_{18}O_{49}$ NWs heterostructures were also successfully synthesized and developed as an efficient photochemical

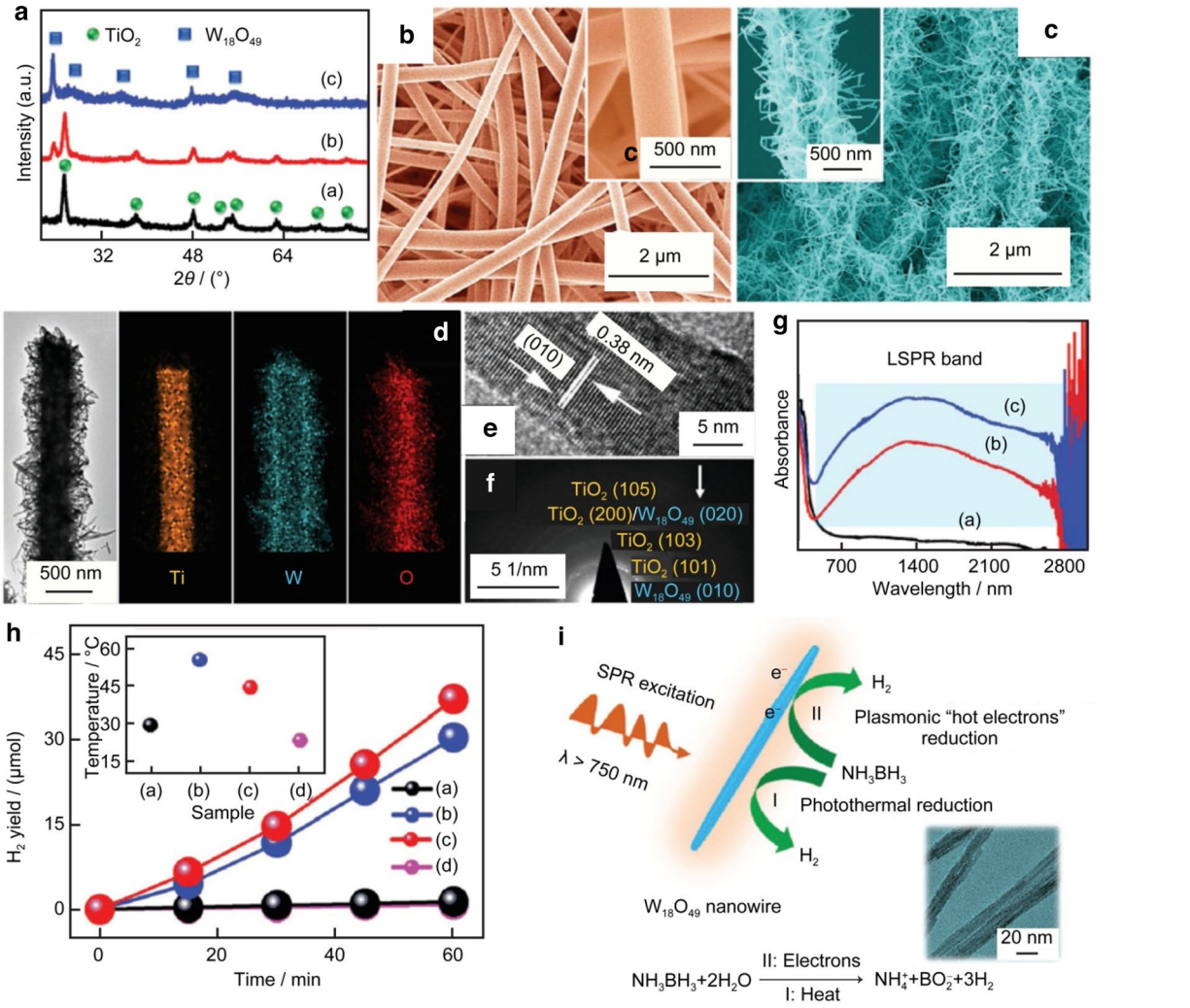


**Fig. 7** **a** XRD patterns of **a** $TiO_2$ NFs, **b** $W_{18}O_{49}/TiO_2$, **c** $W_{18}O_{49}$ NWs. **b**, **c** SEM of $TiO_2$ NFs and $W_{18}O_{49}/TiO_2$. **d** TEM and the corresponding elemental mapping images of an individual $W_{18}O_{49}/TiO_2$ branched heterostructure. **e** HRTEM image of a $W_{18}O_{49}$ NWs. **f** Selected area electron diffraction pattern of the $W_{18}O_{49}/TiO_2$. **g** UV–Vis–IR absorption spectra of the as-fabricated samples. **h** Time-dependent $H_2$ generation from $NH_3BH_3$ aqueous solution over different samples upon IR light irradiation ($\lambda > 750$ nm). **i** Schematic of the catalytic mechanism for $H_2$ generation from $NH_3BH_3$ molecules over the plasmonic $W_{18}O_{49}$ NWs. Reproduced with permission from Ref. [112]. Copyright 2018, Wiley-VCH

catalyst for $H_2$ generation [113]. Under 980 nm irradiation, $H_2$ evolution was 2.11 μmol in 1 h with $NaYF_4$:Yb–Er@$W_{18}O_{49}$ heterostructure. As a comparison, $H_2$ evolution was negligible with $NaYF_4$:Yb–Er NPs and $H_2$ evolution was 0.60 μmol in 1 h with $W_{18}O_{49}$ NWs, which demonstrates the poor catalytic activity of unexcited plasmonic $W_{18}O_{49}$ NWs. As calculated, the NIR-driven catalyst of $Yb^{3+}/Er^{3+}$-doped $NaYF_4/W_{18}O_{49}$ NWs heterostructure achieves a 3.5-fold increase in the catalytic $H_2$ evolution from ammonia borane based on the process of plasmonic energy transfer, which is higher than that of pure $W_{18}O_{49}$ NWs. It was confirmed that the excited LSPR of $W_{18}O_{49}$ NWs could greatly enhance the catalytic $H_2$ evolution, attributed to the plasmonic transfer process of "hot electrons". This work concluded that the upconversion emission of $Ln^{3+}$-doped $NaYF_4$ nanoparticles at a suitable wavelength region can improve the LSPR excitation of the $W_{18}O_{49}$ NWs and boost the catalytic activity for $H_2$ evolution on the surface of $W_{18}O_{49}$ NWs. Such work was considered to be the first demonstration of a high-energy hot electron transfer process in a plasmonic semiconductor heterostructure excited by low-energy IR photons, which stands out as one of the notable landmarks in expanding the photoresponse of current semiconductor photocatalysts from the UV (or Vis) to the IR light range for achieving full-spectrum-driven solar-to-fuel conversion.

Currently, the defect-rich structure and remarkable physicochemical properties make $W_{18}O_{49}$ NWs a potential

candidate for energy conversion, as illustrated in Table 1. However, the efficiency of the $W_{18}O_{49}$ NWs-based catalysts still need to be improved. Obviously, $W_{18}O_{49}$ NWs need to couple with other semiconductor materials to construct hybrid materials to enhance the catalytic activity owing to the unsuitable band edge potential levels. Although surface modification engineering, element doping, and heterostructure assembly have been successfully applied to improve the efficiency of the $W_{18}O_{49}$ NWs-based catalysts, some heterojunctions of $W_{18}O_{49}$ NWs-based catalyst still exist and need to explore well, such as p–n junction, S-scheme, and Schottky barrier.

## 4 $W_{18}O_{49}$ NWs for energy storage

### 4.1 $W_{18}O_{49}$ NWs for rechargeable batteries

Tungsten oxide has been regarded as a promising anode material for lithium-ion batteries due to its larger theoretical capacity and high density (693 $mA{\cdot}h{\cdot}g^{-1}$ and 7.16 $g{\cdot}cm^{-3}$), compared to graphite (372 $mA{\cdot}h{\cdot}g^{-1}$ and 2.26 $g{\cdot}cm^{-3}$) [114]. Generally speaking, anode materials based on conversion reaction mechanism always suffer from significant structural and volume variation during long-term cycle processes, leading to the electrodes' poor cycling ability [115, 116]. The reduction of particle size and surface modification with the conductive material of electrode materials are effective approaches to overcome these problems. For instance, the preparation of nanowire structures has been proved to be an effective method. This section will present the recent progress of $W_{18}O_{49}$ NWs for rechargeable batteries, including anodes, cathodes, and separators.

The carbon layer on the surface of anode materials can act as a protective layer to prevent volume expansion and improve electronic conductivity. Carbon-coated ultrathin $W_{18}O_{49}$ NWs web was synthesized and applied as anode material for high-performance lithium-ion batteries [117]. The morphologies of $W_{18}O_{49}$ and $W_{18}O_{49}$@carbon nanowire are shown in Fig. 8a, b. It was clearly revealed from TEM images that the $W_{18}O_{49}$ NWs were composed of many individual thinner nanowires. The diameter of the $W_{18}O_{49}$ NWs was about 0.9 nm. $W_{18}O_{49}$/C-1 exhibit similar nanowire web morphology with $W_{18}O_{49}$ NWs, and a thin carbon layer with a thickness of about 0.6 nm was coated on the $W_{18}O_{49}$ NWs. As shown in Fig. 8c, the electrochemical test indicated that carbon-coated ultrathin $W_{18}O_{49}$ NWs web presented much better electrochemical performance than pure $W_{18}O_{49}$. It is revealed that the $W_{18}O_{49}$@carbon nanowire web electrode delivered a high lithium storage capacity of 889 $mA{\cdot}h{\cdot}g^{-1}$ at 200 $mA{\cdot}g^{-1}$ after 250 cycles. It was confirmed that excellent electrochemical performance benefited from the incorporation of carbon and the unique ultrathin $W_{18}O_{49}$ nanowire web architecture. Meanwhile, ultrathin $W_{18}O_{49}$ NWs were used to improve the electrochemical performance of Si anode [118]. Schematic of the synthesis and the lithiation process of Si/$W_{18}O_{49}$ electrode is illustrated in Fig. 8d. TEM images showed that $W_{18}O_{49}$ NWs with a length of 200–400 nm and a diameter of 5–10 nm were homogeneously dispersed on the surface of Si nanoparticles, as shown in Fig. 8e. Based on the advantage of the uniform intertwists of ultrathin $W_{18}O_{49}$ NWs structure, $W_{18}O_{49}$ NWs/Si composite exhibited improved reversible capacity and rate capability compared to pure $W_{18}O_{49}$ NWs and Si. It is shown in Fig. 8f that the Si/$W_{18}O_{49}$ NWs-2 with high Si content of 62.5% in the composite presented a higher first capacity of 1379/2228 $mA{\cdot}h{\cdot}g^{-1}$ at 400 $mA{\cdot}g^{-1}$, and retained a reversible capacity of 844 $mA{\cdot}h{\cdot}g^{-1}$ over 100 cycles. It is confirmed that the uniform intertwists of ultrathin nanowires played an effective role in sustaining large lithiation/delithiation strain. This simple strategy will be helpful to design other Si-based and alloy-type anode materials with improved electrochemical performance.

Owing to the favorable defect structure and the novel properties of mixed valency, $W_{18}O_{49}$ was successfully used as functional material for Li–S batteries [119, 120].

**Table 1** Summary of $W_{18}O_{49}$ NWs-based catalyst for fuel production

| Fuel production types | Component | Main product | Main product rate | References |
|---|---|---|---|---|
| $CO_2$ conversion | $W_{18}O_{49}$ NWs | $CH_4$ | 0.029 $mmol{\cdot}L^{-1}\ g^{-1}\ h^{-1}$ | [31] |
| | $W_{18}O_{49}$ NWs @Co | $CO/H_2$ | 21.18 $mmol\ {\cdot}g^{-1}\ h^{-1}$ and 6.49 $mmol\ {\cdot}g^{-1}\ h^{-1}$ | [97] |
| | $Cu^{+}$-doped $W_{18}O_{49}$ NWs | $CH_4$ | 0.67 $\mu mol\ {\cdot}g^{-1}\ h^{-1}$ | [98] |
| | Au/$TiO_2$/$W_{18}O_{49}$ NWs | $CH_4$ | 35.55 $\mu mol{\cdot}\ g^{-1}\ h^{-1}$ | [99] |
| $H_2$ production | $W_{18}O_{49}$ NWs | $H_2$ | 79.5 $\mu mol{\cdot}\ h^{-1}$ | [104] |
| | $W_{18}O_{49}$ NWs/g-$C_3N_4$ | $H_2$ | 3.69 $\mu mol{\cdot}\ h^{-1}$ | [108] |
| | Ag/$W_{18}O_{49}$ NWs | $H_2$ | 2.76 $\mu mol{\cdot}\ h^{-1}$ | [109] |
| | $W_{18}O_{49}$ NWs/$TiO_2$ | $H_2$ | 0.62 $\mu mol\ {\cdot}min^{-1}$ | [112] |
| | $Yb^{3+}$/$Er^{3+}$-doped $NaYF_4$/$W_{18}O_{49}$ NWs | $H_2$ | 2.11 $\mu mol\ {\cdot}h^{-1}$ | [113] |

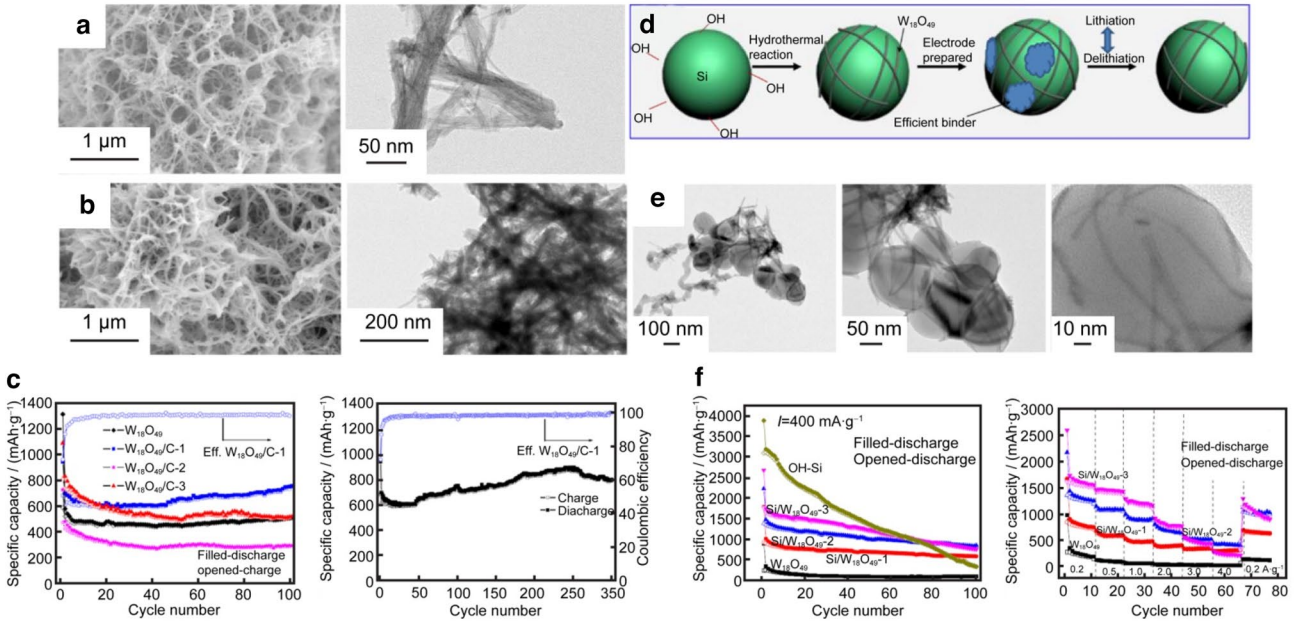


**Fig. 8** **a** SEM and TEM images of $W_{18}O_{49}$ NWs. **b** SEM and TEM images of $W_{18}O_{49}$/C-1. **c** Cycling stability of $W_{18}O_{49}$, $W_{18}O_{49}$/C-1, $W_{18}O_{49}$/C-2 and $W_{18}O_{49}$/C-3 at a rate of 100 mA·g$^{-1}$ and long-term cycling performance of $W_{18}O_{49}$/C-1 at a rate of 200 mA·g$^{-1}$. Reproduced with permission from Ref. [117]. Copyright 2015. The Royal Society of Chemistry. **d** Schematic illustration of the synthesis and the lithiation process of the Si/$W_{18}O_{49}$ electrode. **e** TEM images of Si/$W_{18}O_{49}$. **f** Cycling performances and rate performances of $W_{18}O_{49}$ and Si/$W_{18}O_{49}$ electrodes. Reproduced with permission from Ref. [118]. Copyright 2017, Elsevier

Considerable efforts have been devoted to using $W_{18}O_{49}$ NWs for the improvement and optimization of electrode materials, whereas scarce studies have reported the use of $W_{18}O_{49}$ NWs to improve the electrode structure and cell configuration. Recently, the $W_{18}O_{49}$ NWs were reported as a barrier layer material to alleviate the undesirable shuttle effect for boosting the specific capacity and cycling stability of Li–S batteries [121]. The commercial sulfur cathode with 70% sulfur loading achieved an initial discharge capacity of 1142 mA·h·g$^{-1}$ when $W_{18}O_{49}$ NWs/Super P was used as a barrier layer and retained the specific capacity at about 809 mA·h·g$^{-1}$ after 50 cycles, while an initial specific discharge capacity of 935 mA·h·g$^{-1}$ was obtained when pure Super P was used as the barrier layer. In addition, $W_{18}O_{49}$ NWs were also used as electrocatalysts to improve the electrochemical performance of graphite felt (GF) electrodes in vanadium redox flow batteries (VRFBs) [122]. It was revealed that hydrogen-treated $W_{18}O_{49}$ NWs (H–$W_{18}O_{49}$ NWs)-based VRFBs exhibit outstanding performance with 9.1 and 12.5% higher energy efficiency than the cells assembled with $W_{18}O_{49}$ NWs and treated GF, respectively, at a high current density of 80 mA·cm$^{-2}$. It was confirmed that the superior performance of the H–$W_{18}O_{49}$ NWs electrocatalyst electrode could be attributed to the numerous oxygen vacancies, which can act as active sites for the $VO_2^+/VO^{2+}$ redox reaction. Notably, the VRFBs assembled with the as-prepared hydrogen-treated $W_{18}O_{49}$ NWs-based electrode had high-capacity retention and excellent stability.

Overall, $W_{18}O_{49}$ NWs have been investigated as electrode materials for rechargeable batteries, which show good electrochemical performance. However, it is still a challenge to apply them as anodes for Li-ion batteries because of their large irreversible capacity, low rate capacity, low Coulombic efficiency, and bulky volume expansions during repeated charge intercalation/deintercalation processes. In addition, tungsten is a rare metal. It is not an element abundant on Earth, as required for energy storage applications. Therefore, it is suitable to use $W_{18}O_{49}$ NWs as a functional material for batteries, such as additives and catalysts.

### 4.2 $W_{18}O_{49}$ NWs for supercapacitors

Supercapacitors have attracted much attention due to their significant advantages, such as high power density and ultralong cycle life [123, 124]. Thus, supercapacitors have been considered one of the most effective solutions for the uninterrupted energy supply chain. Recently, many efforts have been devoted to achieving excellent comprehensive performance for supercapacitors, such as exploring new materials and introducing new reaction mechanisms [125–127]. Currently, monoclinic $W_{18}O_{49}$ was discovered as the emerging electrode material for capacitors [128, 129]. $W_{18}O_{49}$ possesses many tunnels in

the crystal structure, including hexagonal tunnels, trigonal tunnels, and quadrilateral tunnels, which are helpful for ion intercalation. Moreover, the high oxygen vacancies content in $W_{18}O_{49}$ structure also can enhance the electrical conductivity by accelerating electron diffusion [34]. With a large surface-to-volume ratio in the 1D structure, massive exposed SOVs on the surface could provide abundant active sites, thus showing the great potential in applications of supercapacitors.

The $W_{18}O_{49}$ NWs/carbon felt (CF) was prepared by a facile solvothermal method and used for supercapacitor applications [130]. Owing to the three-dimensional porous nanostructure and sufficient oxygen deficiencies, the $W_{18}O_{49}$ NWs/CF exhibits a reduction in the resistance and fast reaction kinetics than $WO_3$ NWs /CF. Therefore, $W_{18}O_{49}$ NWs/CF achieved a high capacity of 588.33 $F{\cdot}g^{-1}$ at 1 $A{\cdot}g^{-1}$. Particularly, $W_{18}O_{49}$ NWs/CF presented an excellent cycle performance that can maintain about 88% of its capacitance after 5000 cycles. $W_{18}O_{49}$ NWs/carbon cloth (CC) was synthesized by a simple solvothermal reaction and used as a positive electrode to construct flexible asymmetric supercapacitors [131]. The NWs/CC electrode showed good electrochemical performance with specific capacitance reaching up to 398 $F{\cdot}g^{-1}$ at 2 $A{\cdot}g^{-1}$. Moreover, the NWs/CC electrode presented a specific capacitance of 325 $F{\cdot}g^{-1}$ even at a much higher current density of 6 $A{\cdot}g^{-1}$. After 3000 cycles, the NWs/CC electrode can keep 92% of the initial specific capacitance. The as-fabricated flexible asymmetric supercapacitors (FASCs) based on NWs/CC obtained a high energy density of 28 $Wh{\cdot}kg^{-1}$ and 13 $Wh{\cdot}kg^{-1}$ at a power density of 745 $W{\cdot}kg^{-1}$ and 22.5 $kW{\cdot}kg^{-1}$, respectively. Specifically, the FASCs presented excellent cycle stability and achieved 81% of the specific capacitance after 10,000 cycles.

In addition to the above monovalent cation-based supercapacitors, $W_{18}O_{49}$ NWs were also successfully applied to design trivalent $Al^{3+}$ ion intercalation supercapacitors [132]. As illustrated in Fig. 9a, b, a freestanding composite electrode consisting of uniformly distributed $W_{18}O_{49}$ NWs and single-walled carbon nanotubes (SCNTs) was successfully prepared and applied in $Al^{3+}$ ion intercalation supercapacitors. It is shown in Fig. 9c that the freestanding SCNTs/$W_{18}O_{49}$ NWs-composite film electrode exhibits extremely high areal capacitances of 216 $F{\cdot}g^{-1}$ at 2 $mA{\cdot}cm^{-2}$ due to the highly efficient $Al^{3+}$ ion intercalation into $W_{18}O_{49}$ NWs. To further evaluate the practical potential of composite film for supercapacitors, an Al-ion-based, flexible, asymmetric electrochemical capacitor was constructed. The capacitor presented a high volumetric energy density of 19.0 $mWh{\cdot}cm^{-3}$ at a high power density of 295 $mW{\cdot}cm^{-3}$. Impressively, the asymmetric supercapacitor exhibits excellent cycling stability, which retains 95.9% of its initial capacitance after 6000 cycles. Moreover, the as-prepared supercapacitor was successfully applied to power a flexible poly(3-hexylthiophene)-based electrochromic device (P-ECD), as shown in Fig. 9d, e. The results revealed that the P-ECDs could be switched using a fully charged supercapacitor at a high charge rate of 22 $mA{\cdot}cm^{-2}$, which present a promising capability as a power source for flexible electronic devices. Besides, $W_{18}O_{49}$ NWs–rGO was also used to fabricate an $Al^{3+}$ ion asymmetric supercapacitor [133]. The as-fabricated supercapacitor delivered a high specific capacitance of 365.5 $F{\cdot}g^{-1}$ at 1 $A{\cdot}g^{-1}$ and exhibited excellent cycling stability with 96.7% capacitance retention at 12,000 cycles. More impressively, it demonstrates a high energy density of 28.5 $Wh{\cdot}kg^{-1}$ and a high power density of 751 $W{\cdot}kg^{-1}$.

### 4.3 $W_{18}O_{49}$ NWs for electrochromic energy storage systems

Electrochromic energy storage system is a new type of energy conversion and storage system [134, 135]. The system can demonstrate color alteration and the energy can also be stored directly inside the system. In general, an electrochromic energy storage system consists of two electrodes and an electrolyte. In recent years, two types of electrochromic energy storage systems have been reported, such as electrochromic batteries and electrochromic capacitors [136–138]. Currently, various materials have been developed to fabricate high-performance electrochromic energy storage systems, such as inorganic and conducting polymers [139–142]. To demonstrate color alteration and store energy directly inside the system, the selection of materials is highly important for fabricating a high-performance electrochromic energy storage system [143, 144].

$W_{18}O_{49}$ NWs were successfully applied to design smart supercapacitor, which possesses the capacity to sense changes in the level of stored energy by changing color with variations [145]. As illustrated in Fig. 10a, $W_{18}O_{49}$ NWs and polyaniline (PANI) were successfully employed as components to fabricate electrochromic supercapacitors. The $W_{18}O_{49}$ NWs exhibited high areal capacitances of 440, 360, 333, 315, and 302 $F{\cdot}g^{-1}$ at current densities of 2, 4, 6, 8, and 10 $A{\cdot}g^{-1}$, respectively. It was also indicated from the near-linear charge and discharge slopes that the hybrid electrochromic supercapacitor electrode presented excellent reversibility during the charge–discharge processes. It was revealed that the hybrid supercapacitor obtained an areal capacitance of 10 $mF{\cdot}cm^{-2}$. More impressively, it is illustrated in Fig. 10b that the smart supercapacitor can work in a widened window of 1.3 V while displaying variations in color schemes depending on the level of energy storage, which was distinguished from the conventional capacitor.

In addition, $W_{18}O_{49}$ NWs-based hybrid film electrode was successfully prepared to fabricate electrochromic

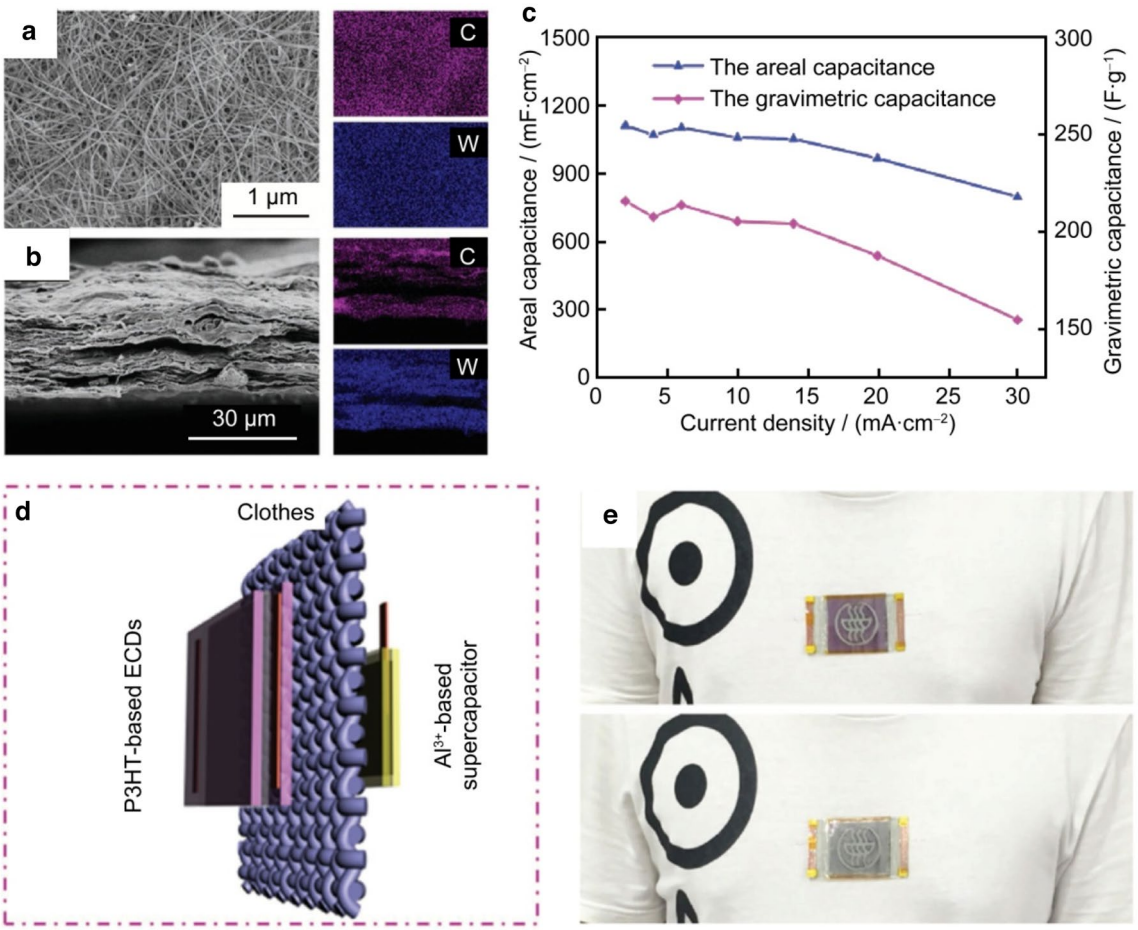


**Fig. 9** Field emission SEM image and EDX elemental maps of the SCNTs)/$W_{18}O_{49}$ NWs-composite films, **a** surface and **b** cross section. **c** Areal capacitances of the composite electrodes under different current densities. **d** Schematic illustration of a wearable P-ECD integrated with a flexible $Al^{3+}$-based supercapacitor as the power source. **e** Corresponding photographs of the wearable P-ECD at the colored and bleached states, respectively. Reproduced with permission from Ref. [132]. Copyright 2017, Wiley-VCH

supercapacitor, which can recognize the level of stored energy with reversible color change [146]. The $W_{18}O_{49}$ NWs/rGO hybrid film electrode presented high conductivity, tunable resistances (23–39 $\Omega \cdot sq^{-1}$), and transmittance (72–84%). Specifically, the $W_{18}O_{49}$ NWs/rGO electrode can maintain its functionalities after 4000 bending cycles. CV test indicated $W_{18}O_{49}$ NWs-based electrode clearly presented pseudocapacitive behavior, which would demonstrate considerable high areal capacitance. It was revealed that the as-fabricated film electrode achieved a high areal capacitance of 92 $mF \cdot cm^{-2}$ at current densities of 2 $mA \cdot cm^{-2}$. Meanwhile, the $W_{18}O_{49}$ NWs/rGO film electrode also presented excellent electrochromic performance, with fast switching speeds (8 s for coloration and 8.45 s for bleaching), and high coloration efficiency (46 $cm^2 \cdot C^{-1}$), and remarkable stability (96.41% of the original optical modulation). A symmetric electrochromic supercapacitor based on $W_{18}O_{49}$ NWs/rGO film electrode delivered a maximum areal capacitance of 48 $mF \cdot cm^{-2}$ and an energy density of 5.2 $mWh \cdot cm^{-2}$ with 0.391 $mW \cdot cm^{-2}$ power density. In particular, the device exhibited excellent mechanical flexibility and stability over 4000 cycles during the charge/discharge process. More impressively, the dual-functional supercapacitor exhibited a rapid and reversible response and high sustainability in optical modulation (96%) even under high current charge/discharge conditions, which is promising for real applications. Moreover, $W_{18}O_{49}$ NWs/rGO and PANI electrodes were also used to assemble an electrochromic supercapacitor [147]. $W_{18}O_{49}$ NWs/rGO film electrode exhibited a specific capacitance of 15.06 $mF \cdot cm^{-2}$ at current densities of 0.2 $mA \cdot cm^{-2}$. The PANI electrode presented a high specific capacitance of 62.26 $mF \cdot cm^{-2}$ at a discharge current of 0.2 $mA \cdot cm^{-2}$. As illustrated in Fig. 10c, d, the assembled device exhibited various color changes at the voltage of − 0.2 to 1.4 V, such as light green, dark green, light blue, and dark blue. The coloring efficiency reached 76.37 $cm^{-2}\ C^{-1}$. It was believed that these creative supercapacitors equipped with smart functionalities

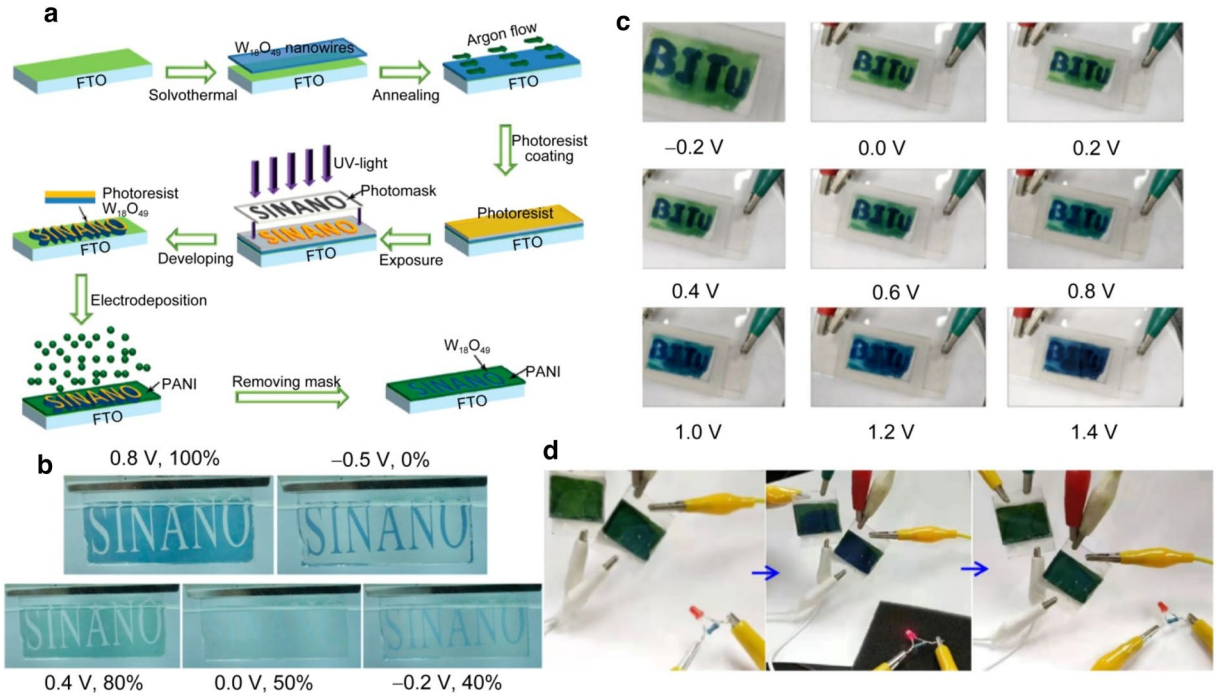


**Fig. 10** **a** Schematic of the process of fabricating a supercapacitor electrode composed of $W_{18}O_{49}$ NWs and a PANI layer. **b** Images of the supercapacitor electrode at several typical states demonstrating the stored energy conveyed through pattern color scheme recognition. Reproduced with permission from Ref. [145]. Copyright 2014, American Chemical Society. **c** Digital photo of $W_{18}O_{49}$ NWs/rGO and PANI-based electrochromic supercapacitor at different voltages. **d** Two electrochromic supercapacitors were integrated to power an LED. Reproduced with permission from Ref. [147]. Copyright 2021, Springer

could effectively meet the needs of humans in providing connectivity and delivering relevant information.

Obviously, $W_{18}O_{49}$ NWs have been successfully applied as electrode for supercapacitors and electrochromic supercapacitors, as illustrated in Table 2. However, the specific capacitance and cycle life of the $W_{18}O_{49}$ NWs-based supercapacitors still need to be improved. Although the method of using $W_{18}O_{49}$ NWs to couple with conductive materials to construct hybrid materials has been successfully applied to improve the capacitance of the $W_{18}O_{49}$ NWs-based electrode, other existing methods, such as surface modification engineering, element doping, and heterostructure assembly, still need to be well explored.

## 5 Conclusion and perspectives

In conclusion, $W_{18}O_{49}$ NWs have demonstrated their enormous potential in the development of highly efficient energy conversion and storage systems due to their unique physicochemical properties and excellent electrochemical performances. Although considerable achievements are made, more efforts are still needed to further promote the fundamental understanding and practical applications of $W_{18}O_{49}$ NWs. Moreover, the synthesis of large-scale $W_{18}O_{49}$ NWs with high quality using more environmentally friendly and low-cost methods is still challenging,

**Table 2** Summary of $W_{18}O_{49}$ NWs-based materials for supercapacitors

| Energy storage types | Component | Preparation method | Specific capacitance | Cycle life | References |
|---|---|---|---|---|---|
| Supercapacitors | $W_{18}O_{49}$ NWs/CF | Solvothermal | 588.33 $F{\cdot}g^{-1}$ | 5000 | [130] |
| | $W_{18}O_{49}$ NWs/CC | Solvothermal | 325 $F{\cdot}g^{-1}$ | 3000 | [131] |
| | $W_{18}O_{49}$ NWs/SCNTs | Solvothermal | 216 $F{\cdot}g^{-1}$ | 6000 | [132] |
| | $W_{18}O_{49}$ NWs–rGO | Solvothermal | 365.5 $F{\cdot}g^{-1}$ | 12,000 | [133] |
| | $W_{18}O_{49}$ NWs–PANI | Solvothermal | 440 $F{\cdot}g^{-1}$ | – | [145] |
| | $W_{18}O_{49}$ NWs/rGO | Solvothermal | 92 $mF{\cdot}cm^{-2}$ | 4000 | [146] |
| | $W_{18}O_{49}$ NWs–rGO | Solvothermal | 15.06 $mF{\cdot}cm^{-2}$ | – | [147] |

and there is undoubtedly plenty of room for improvement. Meanwhile, there are practical challenges that must be overcome to meet the energy needs of the next-generation power systems, including long-term cycling stability, superior energy and power capabilities, high rate performance, low price, and environmental friendliness. Many important concerns have to be considered, and further improvements must be made in the expansion of future $W_{18}O_{49}$ NWs-based materials for energy storage applications. Some prospects for further research of $W_{18}O_{49}$ NWs in energy conversion and storage are presented.

Firstly, future research should focus on ultralong $W_{18}O_{49}$ NWs. Ultralong $W_{18}O_{49}$ NWs with lengths larger than 100 μm and diameters smaller than 10 nm exhibit many superior properties to those of short-length $W_{18}O_{49}$ NWs. So developing new, low-cost, and environmentally friendly synthetic methods which are suitable for mass production of ultralong $W_{18}O_{49}$ NWs is necessary. The growth mechanisms of $W_{18}O_{49}$ NWs need to be further investigated; especially, the details of the growth mechanisms that occur during the synthesis of ultralong $W_{18}O_{49}$ NWs are still elusive.

Secondly, the low energy density of $W_{18}O_{49}$ NWs-based electrodes cannot meet the requirements of portable electronics. Therefore, further investigations should be aimed at improving their energy density. Besides, although numerous experiments have been conducted to understand the catalytic mechanism of $W_{18}O_{49}$ NWs during the last decade, a universally accepted catalytic mechanism is desired to guide the design and applications of $W_{18}O_{49}$ NWs.

Thirdly, $W_{18}O_{49}$ NWs can be explored for promising multifunctional devices. The successful experiences of $W_{18}O_{49}$ NWs applied in rechargeable batteries, capacitors, and electrochromic energy storage systems could be used for reference for fabricating new energy-related devices, such as photo-assisted rechargeable metal batteries and solar rechargeable batteries [148, 149].

Finally, large-scale production of $W_{18}O_{49}$ NWs needs to be studied for practical applications. The development of $W_{18}O_{49}$ NWs is just in the middle stage. The yield of $W_{18}O_{49}$ NWs for scalable fabrication is still insufficient, and producing $W_{18}O_{49}$ NWs with various structures is still costly. It is believed that the application of $W_{18}O_{49}$ NWs would be further extended from a simple laboratory process to device-oriented design and control. Therefore, environmentally friendly and low-cost preparative techniques for large-scale $W_{18}O_{49}$ NWs with high quality are urgently needed.

**Acknowledgements** Financial support from the National Natural Science Foundation (No. 22075151) of China, the Natural Science Foundation of Jiangxi (No. 20161BBE50095) and the project of Jiangxi Academy of Sciences (No. 2022YSBG21019 and No. 2023YJC2018) is gratefully acknowledged.

**Data availability** The data that support this study are available from the corresponding author, upon reasonable request.

## Declarations

**Conflict of interest** The authors declare no conflict of interest.

## References

1. Rogelj J, Huppmann D, Krey V, Riahi K, Clarke L, Gidden M, Nicholls Z, Meinshausen M. A new scenario logic for the Paris agreement long-term temperature goal. Nature. 2019;573:357.
2. Pilpola S, Arabzadeh V, Mikkola J, Lund PD. Analyzing national and local pathways to carbon-neutrality from technology, emissions, and resilience perspectives case of Finland. Energies. 2019;12:949.
3. Chi YY, Liu ZR, Wang X, Zhang YY, Wei F. Provincial $CO_2$ emission measurement and analysis of the construction industry under China's carbon neutrality target. Sustainability. 2021;13:1876.
4. Liu Z, Deng Z, He G, Wang HL, Zhang X, Lin J, Qi Y, Liang X. Challenges and opportunities for carbon neutrality in China. Nat Rev Earth Environ. 2022;3:141.
5. Zhao X, Ma XW, Chen BY, Shang YP, Song ML. Challenges toward carbon neutrality in China: strategies and countermeasures. Resour Conserv Recy. 2022;176: 105959.
6. Kruitwagen L, Story KT, Friedrich J, Byers L, Skillman S, Hepburn C. A global inventory of photovoltaic solar energy generating units. Nature. 2021;598:604.
7. Moriarty P, Honnery D. Intermittent renewable energy: the only future source of hydrogen? Int J Hydrog Energy. 2007;32:1616.
8. Lewis NS, Nocera DG. Powering the planet: chemical challenges in solar energy utilization. Proc Natl Acad Sci. 2006;103:15729.
9. Zhang L, Wang H, Liu JB, Zhang QQ, Yan H. Nonstoichiometric tungsten oxide: structure, synthesis, and applications. J Mater Sci Mater Electron. 2020;31:861.
10. Huang ZF, Song J, Pan L, Zhang X, Wang L, Zou JJ. Tungsten oxides for photocatalysis, electrochemistry, and phototherapy. Adv Mater. 2015;27:5309.
11. Shinde PA, Jun SC. Review on recent progress in the development of tungsten oxide based electrodes for electrochemical energy storage. Chemsuschem. 2020;13:11.
12. Yin S, Asakura Y. Recent research progress on mixed valence state tungsten based materials. Tungsten. 2019;1:5–18.
13. Wang SC, Wang LZ. Recent progress of tungsten- and molybdenum-based semiconductor materials for solar-hydrogen production. Tungsten. 2019;1:19.
14. Wang JL, Lu YR, Li HH, Liu JW, Yu SH. Large area co-assembly of nanowires for flexible transparent smart windows. J Am Chem Soc. 2017;139:9921.
15. Wang JL, Sheng SZ, He Z, Wang R, Pan Z, Zhao HY, Liu JW, Yu SH. Self-powered flexible electrochromic smart window. Nano Lett. 2021;21:9976.
16. Liu JW, Zheng J, Wang JL, Xu J, Li HH, Yu SH. Ultrathin $W_{18}O_{49}$ nanowire assemblies for electrochromic devices. Nano Lett. 2013;13:3589.
17. Lu CH, Hon MH, Kuan CY, Leu IC. Controllable synthesis of $W_{18}O_{49}$ nanowire arrays and their application in electrochromic devices. J Mater Sci. 2015;50:5739.
18. Gu HX, Guo CS, Zhang SH, Bi LH, Li TC, Sun TD, Liu SQ. Highly efficient, near-infrared and visible light modulated

electrochromic devices based on polyoxometalates and $W_{18}O_{49}$ nanowires. ACS Nano. 2018;12:559.
19. Chen ZG, Wang Q, Wang HL, Zhang LS, Song GS, Song LL, Hu JQ, Wang HZ, Liu JS, Zhu MF, Zhao DY. Ultrathin PEGylated $W_{18}O_{49}$ nanowires as a new 980 nm-laser-driven photothermal agent for efficient ablation of cancer cells in vivo. Adv Mater. 2013;25:2095.
20. Xu WJ, Tian QY, Chen ZG, Xia MG, Macharia DK, Sun B, Tian L, Wang YF, Zhu MF. Optimization of photothermal performance of hydrophilic $W_{18}O_{49}$ nanowires for the ablation of cancer cells in vivo. J Mater Chem B. 2014;2:5594.
21. Wang XY, Li J, Shen YH, Xie AJ. An assembled ordered $W_{18}O_{49}$ nanowire film with high SERS sensitivity and stability for the detection of RB. Appl Surf Sci. 2020;504: 144073.
22. Xu YS, Ma TT, Zhao YQ, Zheng LL, Liu XH, Zhang J. Multimetal functionalized tungsten oxide nanowires enabling ultrasensitive detection of triethylamine. Sens Actuators B Chem. 2019;300: 127042.
23. Zhao YM, Zhu YQ. Room temperature ammonia sensing properties of $W_{18}O_{49}$ nanowires. Sens Actuators B Chem. 2009;137:27.
24. Yang F, Huang K, Ni SB, Wang Q, He DY. $W_{18}O_{49}$ nanowires as ultraviolet photodetector. Nanoscale Res Lett. 2010;5:416.
25. Xiao Y, Tao XQ, Qiu GH, Dai ZF, Gao P, Li BX. Optimal synthesis of a direct Z-scheme photocatalyst with ultrathin $W_{18}O_{49}$ nanowires on g-$C_3N_4$ nanosheets for solar-driven oxidation reactions. J Colloid Interface Sci. 2019;550:99.
26. Qiu P, Huang C, Dong G, Chen FY, Zhao FF, Yu YS, Liu XQ, Li Z, Wang Y. Plasmonic gold nanocrystals simulated efficient photocatalytic nitrogen fixation over Mo doped $W_{18}O_{49}$ nanowires. J Mater Chem A. 2021;9:14459.
27. Huang ZF, Song J, Pan L, Jia X, Li Z, Zou JJ, Zhang X, Wang L. $W_{18}O_{49}$ nanowire alignments with a BiOCl shell as an efficient photocatalyst. Nanoscale. 2014;6:8865.
28. Bhavania P, Kumarb P, Hussainc M, Jeond KJ, Park YK. Recent advances in wide solar spectrum active W18O49-based photocatalysts for energy and environmental applications. Catal Rev. 2022. https://doi.org/10.1080/01614940.2022.2038472.
29. Frey GL, Rothschild A, Sloan J, Rosentsveig R, Popovitz-Biro R, Tenne R. Investigations of nonstoichiometric tungsten oxide nanoparticles. J Solid State Chem. 2001;162:300.
30. Viswanathan K, Brandt K, Salje E. Crystal structure and charge carrier concentration of $W_{18}O_{49}$. J Solid State Chem. 1981;36:45.
31. Xi GC, Ouyang SX, Li P, Ye JH, Ma Q, Su N, Bai H, Wang C. Ultrathin $W_{18}O_{49}$ nanowires with diameters below 1 nm: synthesis, near-infrared absorption, photoluminescence, and photochemical reduction of carbon dioxide. Angew Chem Int Edit. 2012;51:2395.
32. Migas DB, Shaposhnikov VL, Borisenko VE. Tungsten oxides. II. The metallic nature of Magnéli phases. J Appl Phys. 2010;108:093714.
33. Bandi S, Srivastav AK. Review: Oxygen-deficient tungsten oxides. J Mater Sci. 2021;56:6615.
34. Sinha L, Shirage PM. Surface oxygen vacancy formulated energy storage application: pseudocapacitor-battery trait of $W_{18}O_{49}$ nanorods. J Electrochem Soc. 2019;166:A3496.
35. Sun Y, Wang W, Qin JW, Zhao D, Mao BG, Xiao Y, Cao MH. Oxygen vacancy-rich mesoporous $W_{18}O_{49}$ nanobelts with ultrahigh initial Coulombic efficiency toward high-performance lithium storage. Electrochim Acta. 2016;187:329.
36. Chen ZY, Ye KQ, Li ML, Zhao S, Luo J, Wu B. Lithiation mechanism of $W_{18}O_{49}$ anode material for lithium-ion batteries: experiment and first-principles calculations. J Electroanal Chem. 2021;880: 114885.
37. Martinez-de la Cruz A, Amador U, Rodriguez-Carvajal J, Garcia-Alvarado F. Electrochemical zinc insertion into $W_{18}O_{49}$: synthesis and characterization of new bronzes. J Solid State Chem. 2005;178:2998.
38. Zhao YY, Tang QW, Yang PZ, He BL. Robust electrocatalysts from metal doped $W_{18}O_{49}$ nanofibers for hydrogen evolution. Chem Commun. 2017;53:4323.
39. Zhao YY, Tang QW, He BL, Yang PZ. Mo incorporated $W_{18}O_{49}$ nanofibers as robust electrocatalysts for high-efficiency hydrogen evolution. Int J Hydrogen Energy. 2017;42:14534.
40. Zhang Q, Chakraborty AK, Lee WI. $W_{18}O_{49}$ and $WO_3$ nanorod arrays prepared by AAO-templated electrodeposition method. B Korean Chem Soc. 2009;30:227.
41. Lou XW, Zeng HC. An inorganic route for controlled synthesis of $W_{18}O_{49}$ nanorods and nanofibers in solution. Inorg Chem. 2003;42:6169.
42. Choi HG, Jung YH, Kim DK. Solvothermal synthesis of tungsten oxide nanorod/nanowire/nanosheet. J Am Ceram Soc. 2005;88:1684.
43. Wang D, Li J, Cao X, Pang GS, Feng SH. Hexagonal mesocrystals formed by ultra-thin tungsten oxide nanowires and their electrochemical behaviour. Chem Commun. 2010;46:7718.
44. Liu JC, Margeat O, Dachraoui W, Liu XJ, Fahlman M, Ackermann J. Gram-scale synthesis of ultrathin tungsten oxide nanowires and their aspect ratio-dependent photocatalytic activity. Adv Funct Mater. 2014;24:6029.
45. Zhou HW, Shi YT, Dong QS, Wang YX, Zhu C, Wang L, Wang N, Wei Y, Tao SY, Ma TL. Interlaced $W_{18}O_{49}$ nanofibers as a superior catalyst for the counter electrode of highly efficient dye-sensitized solar cells. J Mater Chem A. 2014;2:4347.
46. Hong KQ, Xie MH, Wu HS. Tungsten oxide nanowires synthesized by a catalyst-free method at low temperature. Nanotechnology. 2006;17:4830.
47. Li YB, Bando Y, Golberg D. Quasi-aligned single-crystalline $W_{18}O_{49}$ nanotubes and nanowires. Adv Mater. 2003;15:1294.
48. Hong KQ, Xie MH, Hu R, Wu HS. Synthesizing tungsten oxide nanowires by a thermal evaporation method. Appl Phys Lett. 2007;90: 173121.
49. Gao XQ, Xiao F, Yang C, Wang JD, Su XT. Hydrothermal fabrication of $W_{18}O_{49}$ nanowire networks with superior performance for water treatment. J Mater Chem A. 2013;1:5831.
50. Chen H, Cai W, Gao X, Luo J, Su X. PABA-assisted hydrothermal fabrication of $W_{18}O_{49}$ nanowire networks and its transition to $WO_3$ for photocatalytic degradation of methylene blue. Adv Powder Technol. 2018;29:1272.
51. Zhang N, Zhao Y, Lu Y, Zhu G. Preparation of aligned $W_{18}O_{49}$ nanowire clusters with high photocatalytic activity. Mater Sci Eng B Adv Funct Solid-State Mater. 2017;218:51.
52. Seelaboyina R, Huang J, Park J, Kang DH, Choi AB. Multistage field enhancement of tungsten oxide nanowires and its field emission in various vacuum conditions. Nanotechnology. 2006;17:4840.
53. Huang R, Zhu J, Yu R. Synthesis and electrical characterization of tungsten oxide nanowires. Chin Phys B. 2009;18:3024.
54. Hsieh YT, Hsueh SH, Chen US, Huang MW, Shih HC. Rapid synthesis of bundled tungsten oxide nanowires by microwave plasma-enhanced chemical vapor deposition and their optical properties. J Electrochem Soc. 2010;157:K183.
55. Xiao ZD, Zhang LD, Tian XK, Fang XS. Fabrication and structural characterization of porous tungsten oxide nanowires. Nanotechnology. 2005;16:2647.
56. Nayak AK, Pradhan D. Microwave-assisted greener synthesis of defect-rich tungsten oxide nanowires with enhanced photocatalytic and photoelectrochemical performance. J Phys Chem C. 2018;122:3183.

57. Shen G, Bando Y, Golberg D, Zhou C. Electron-beam-induced synthesis and characterization of $W_{18}O_{49}$ nanowires. J Phys Chem C. 2008;112:5856.
58. Chen CL, Mori H. In situ TEM observation of the growth and decomposition of monoclinic $W_{18}O_{49}$ nanowires. Nanotechnology. 2009;20: 285604.
59. Yu KS, Pan XL, Zhang GB, Liao XB, Zhou XB, Yan MY, Xu L, Mai LQ. Nanowires in energy storage devices: structures, synthesis, and applications. Adv Energy Mater. 2018;8:1802369.
60. Jin YZ, Zhu YQ, Whitby RLD, Yao N, Ma RZ, Watts PCP, Kroto HW, Walton DRM. Simple approaches to quality large-scale tungsten oxide nanoneedles. J Phys Chem B. 2004;108:15572.
61. Shi SL, Xue XY, Feng P, Liu YG, Zhao H, Wang TH. Low-temperature synthesis and electrical transport properties of $W_{18}O_{49}$ nanowires. J Cryst Growth. 2008;310:462.
62. Gillet M, Delamare R, Gillet E. Growth of epitaxial tungsten oxide nanorods. J Cryst Growth. 2005;279:93.
63. Xu F, Tse SD, Al-Sharab JF, Kear BH. Flame synthesis of aligned tungsten oxide nanowires. Appl Phys Lett. 2006;88: 243115.
64. Zhang Y, Chen YG, Liu HQ, Zhou YQ, Li RY, Cai M, Sun XL. Three-dimensional hierarchical structure of single crystalline tungsten oxide nanowires: construction, phase transition, and voltammetric behavior. J Phys Chem C. 2009;113:1746.
65. Bandi S, Srivastav AK. Unraveling the growth mechanism of $W_{18}O_{49}$ nanowires on W surfaces. CrystEngComm. 2021;23:6559.
66. Burschka J, Pellet N, Moon SJ, Humphry-Baker R, Gao P, Nazeeruddin MK, Graetzel M. Sequential deposition as a route to high-performance perovskite-sensitized solar cells. Nature. 2013;499:316.
67. Jeong M, Choi IW, Go EM, Cho Y, Kim M, Lee B, Jeong S, Jo Y, Choi HW, Lee J, Bae JH, Kwak SK, Kim DS, Yang C. Stable perovskite solar cells with efficiency exceeding 24.8% and 0.3-V voltage loss. Science. 2020;369:1615.
68. Meng LX, Zhang YM, Wan XJ, Li CX, Zhang X, Wang YB, Ke X, Xiao Z, Ding LM, Xia RX, Yip HL, Cao Y, Chen YS. Organic and solution-processed tandem solar cells with 17.3% efficiency. Science. 2018;361:1094.
69. Meng HF, Liao CT, Deng M, Xu XP, Yu LY, Peng Q. 1877 % efficiency organic solar cells promoted by aqueous solution processed cobalt(II) acetate hole transporting layer. Angew Chem Int Edit. 2021;60:22554.
70. Kim M, Jeong J, Lu H, Lee TK, Eickemeyer FT, Liu Y, Choi IW, Choi SJ, Jo Y, Kim HB, Mo SI, Kim YK, Lee H, An NG, Cho S, Tress WR, Zakeeruddin SM, Hagfeldt A, Km JY, Gratzel M, Kim DS. Conformal quantum dot-$SnO_2$ layers as electron transporters for efficient perovskite solar cells. Science. 2022;375:302.
71. Li C, Zhou J, Song JD, Xu JL, Zhang HT, Zhang XN, Guo J, Zhu L, Wei DH, Han GC, Min J, Zhang Y, Xie ZQ, Yi YP, Yan H, Gao F, Liu F, Sun YM. Non-fullerene acceptors with branched side chains and improved molecular packing to exceed 18% efficiency in organic solar cells. Nat Energy. 2021;6:605.
72. You JB, Meng L, Song TB, Guo TF, Yang Y, Chang WH, Hong ZR, Chen H, Zhou HP, Chen Q, Liu YS, De Marco N, Yang Y. Improved air stability of perovskite solar cells via solution-processed metal oxide transport layers. Nat Nanotechnol. 2016;11:75.
73. Chen SS, Dai XZ, Xu S, Jiao HY, Zhao L, Huang JS. Stabilizing perovskite-substrate interfaces for high-performance perovskite modules. Science. 2021;373:902.
74. Li XD, Zhang WX, Guo XM, Lu CY, Wei JY, Fang JF. Constructing heterojunctions by surface sulfidation for efficient inverted perovskite solar cells. Science. 2022;375:434.
75. Oregan B, Gratzel M. A low-cost, high-efficiency solar-cell based on dye-sensitized colloidal $TIO_2$ films. Nature. 1991;353:737.
76. Yun SN, Hagfeldt A, Ma T. Pt-free counter electrode for dye-sensitized solar cells with high efficiency. Adv Mater. 2014;26:6210.
77. Wu MX, Lin X, Hagfeldt A, Ma TL. Low-cost molybdenum carbide and tungsten carbide counter electrodes for dye-sensitized solar cells. Angew Chem Int Edit. 2011;50:3520.
78. Wu MX, Lin X, Wang YD, Wang L, Guo W, Qu DD, Peng XQ, Hagfeldt A, Graetzel M, Ma TL. Economical Pt-free catalysts for counter electrodes of dye-sensitized solar cells. J Am Chem Soc. 2012;134:3419.
79. Li DM, Li H, Luo YH, Li KX, Meng QB, Armand M, Chen LQ. Non-corrosive, non-absorbing organic redox couple for dye-sensitized solar cells. Adv Funct Mater. 2010;20:3358.
80. Tian HN, Gabrielsson E, Yu Z, Hagfeldt A, Kloo L, Sun LC. A thiolate/disulfide ionic liquid electrolyte for organic dye-sensitized solar cells based on Pt-free counter electrodes. Chem Commun. 2011;47:10124.
81. Zhang TH, Liu YF, Yun SN. Recent advances in counter electrodes for thiolate-mediated dye-sensitized solar cells. Isr J Chem. 2015;55:943.
82. Zhou HW, Shi YT, Dong QS, Lin J, Wang AQ, Ma TL. Surface oxygen vacancy-dependent electrocatalytic activity of $W_{18}O_{49}$ nanowires. J Phys Chem C. 2014;118:20100.
83. Zhou HW, Shi YT, Dong QS, Wang L, Zhang H, Ma TL. High electrocatalytic activity of W18O49 nanowires for cobalt complex and ferrocenium redox mediators. RSC Adv. 2014;4:42190.
84. Sui SY, Liao YP, Xie Y, Wang XW, Li L, Luo ZS, Zhou W, Wang GF, Pan K, Cabot A. High catalytic activity of $W_{18}O_{49}$ nanowire-reduced graphite oxide composite counter electrode for dye-sensitized solar cells. ChemistrySelect. 2017;2:8927.
85. You LZ, Liu B, Liu T, Fan BB, Cai YH, Guo L, Sun YM. Organic solar cells based on $WO_{2.72}$ nanowire anode buffer layer with enhanced power conversion efficiency and ambient stability. ACS Appl Mater Interfaces. 2017;9:12629.
86. Zhao YY, Gao L, Wang QR, Gao KD, Mu MF, Tang QW. Robust tungsten oxide nanostructure for efficient photoelectric conversion and hydrogen evolution. Mater Lett. 2022;312: 131626.
87. Saha MS, Banis MN, Zhang Y, Li R, Sun X, Cai M, Wagner FT. Tungsten oxide nanowires grown on carbon paper as Pt electrocatalyst support for high performance proton exchange membrane fuel cells. J Power Sources. 2009;192:330.
88. Saha MS, Zhang Y, Cai M, Sun X. Carbon-coated tungsten oxide nanowires supported Pt nanoparticles for oxygen reduction. Int J Hydrogen Energ. 2012;37:4633.
89. Karim NA, Kamarudin SK, Shyuan LK, Yaakob Z, Daud WRW, Kadhum AAH. Study on the electronic properties and molecule adsorption of $W_{18}O_{49}$ nanowires as a catalyst support in the cathodes of direct methanol fuel cells. J Power Sources. 2015;288:461.
90. Karim NA, Kamarudin SK. Novel heat-treated cobalt phthalocyanine/carbon–tungsten oxide nanowires (CoPc/C–$W_{18}O_{49}$) cathode catalyst for direct methanol fuel cell. J Electroanal Chem. 2017;803:19.
91. Karim NA, Kamarudin SK, Loh KS. Performance of a novel non-platinum cathode catalyst for direct methanol fuel cells. Energ Conver Manage. 2017;145:293.
92. Mittal D, Ahlawat M, Rao VG. Recent progress and challenges in plasmon-mediated reduction of $CO_2$ to chemicals and fuels. Adv Mater Interfaces. 2022;9:2102383.
93. Kibria MG, Edwards JP, Gabardo CM, Cao-Thang D, Seifitokaldani A, Sinton D, Sargent EH. Electrochemical $CO_2$ reduction into chemical feedstocks: from mechanistic electrocatalysis models to system design. Adv Mater. 2019;31:1807166.
94. Wu JH, Huang Y, Ye W, Li YG. $CO_2$ Reduction: from the electrochemical to photochemical approach. Adv Sci. 2017;4:1700194.

95. Asadi M, Kim K, Liu C, Addepalli AV, Abbasi P, Yasaei P, Phillips P, Behranginia A, Cerrato JM, Haasch R, Zapol P, Kumar B, Klie RF, Abiade J, Curtiss LA, Salehi-Khojin A. Nanostructured transition metal dichalcogenide electrocatalysts for $CO_2$ reduction in ionic liquid. Science. 2016;353:467.
96. Lin S, Diercks CS, Zhang YB, Kornienko N, Nichols EM, Zhao Y, Paris AR, Kim D, Yang P, Yaghi OM, Chang CJ. Covalent organic frameworks comprising cobalt porphyrins for catalytic $CO_2$ reduction in water. Science. 2015;349:1208.
97. Zhang HB, Wang Y, Zuo SW, Zhou W, Zhang J, Lou XWD. Isolated cobalt centers on $W_{18}O_{49}$ nanowires perform as a reaction switch for efficient $CO_2$ photoreduction. J Am Chem Soc. 2021;143:2173.
98. Zhang MM, Cheng G, Wei Y, Wen ZP, Chen R, Xiong JY, Li W, Han C, Li Z. Cuprous ion ($Cu^+$) doping induced surface/interface engineering for enhancing the $CO_2$ photoreduction capability of $W_{18}O_{49}$ nanowires. J Colloid Interface Sci. 2020;572:306.
99. Jiang XY, Huang JD, Bi ZH, Ni WJ, Gurzadyan G, Zhu YA, Zhang ZY. Plasmonic active "hot spots"-confined photocatalytic $CO_2$ reduction with high selectivity for $CH_4$ production. Adv Mater. 2022;34:2109330.
100. Chen XB, Shen SH, Guo LJ, Mao SS. Semiconductor-based photocatalytic hydrogen generation. Chem Rev. 2010;110:6503.
101. Zou XX, Zhang Y. Noble metal-free hydrogen evolution catalysts for water splitting. Chem Soc Rev. 2015;44:5148.
102. Nishiyama H, Yamada T, Nakabayashi M, Maehara Y, Yamaguchi M, Kuromiya Y, Nagatsuma Y, Tokudome H, Akiyama S, Watanabe T, Narushima R, Okunaka S, Shibata N, Takata T, Hisatomi T, Domen K. Photocatalytic solar hydrogen production from water on a 100$m^2$ scale. Nature. 2021;598:304.
103. Turner JA. Sustainable hydrogen production. Science. 2004;305:972.
104. Lou Z, Gu Q, Xu L, Liao Y, Xue C. Surfactant-free synthesis of plasmonic tungsten oxide nanowires with visible-light-enhanced hydrogen generation from ammonia borane. Chem Asian J. 2015;10:1291.
105. Lu N, Zhang ZY, Wang Y, Liu BK, Guo L, Wang L, Huang JD, Liu KC, Dong B. Direct evidence of IR-driven hot electron transfer in metal-free plasmonic $W_{18}O_{49}$/Carbon heterostructures for enhanced catalytic $H_2$ production. Appl Catal B Environ. 2018;233:19.
106. Shen CH, Wen XJ, Fei ZH, Liu ZT, Mu QM. Novel Z-scheme $W_{18}O_{49}/CeO_2$ heterojunction for improved photocatalytic hydrogen evolution. J Colloid Interface Sci. 2020;579:297.
107. Hong I, Chen YA, Hsu YJ, Yong K. Triple-channel charge transfer over $W_{18}O_{49}$/Au/g-C3N4 Z-scheme photocatalysts for achieving broad-spectrum solar hydrogen production. ACS Appl Mater Interfaces. 2021;13:52670.
108. Song KN, Xiao F, Zhang LJ, Yue F, Liang XY, Wang JD, Su XT. $W_{18}O_{49}$ nanowires grown on g-$C_3N_4$ sheets with enhanced photocatalytic hydrogen evolution activity under visible light. J Mol Catal A Chem. 2016;418:95.
109. Liu Y, Zhang Z, Fang Y, Liu B, Huang J, Miao F, Bao Y, Dong B. IR-Driven strong plasmonic-coupling on Ag nanorices/$W_{18}O_{49}$ nanowires heterostructures for photo/thermal synergistic enhancement of $H_2$ evolution from ammonia borane. Appl Catal B Environ. 2019;252:164.
110. Yang Y, Cong Y, Cao BS, Xiao Y, Shang JY, Tong Y, Zhang HM, Liu Y, Dong B, Zhang JH. Enhanced core-shell $CeO_2$:Er, Yb@$_{W1}8_{O4}9$ heterojunction $_H2$ generation by multiband emissions of Er ions. Nanotechnology. 2020;31: 165707.
111. Zhong X, Sun Y, Chen X, Zhuang G, Li X, Wang JG. Mo doping induced more active sites in urchin-like $W_{18}O_{49}$ nanostructure with remarkably enhanced performance for hydrogen evolution reaction. Adv Funct Mater. 2016;26:5778.
112. Zhang ZY, Jiang XY, Liu BK, Guo JL, Lu N, Wang L, Huang JD, Liu KC, Dong B. IR-driven ultrafast transfer of plasmonic hot electrons in nonmetallic branched heterostructures for enhanced $H_2$ generation. Adv Mater. 2018;30:1705221.
113. Zhang ZY, Liu Y, Fang YR, Cao BS, Huang JD, Liu KC, Dong B. Near-infrared-plasmonic energy upconversion in a nonmetallic heterostructure for efficient $H_2$ evolution from ammonia borane. Adv Sci. 2018;5:1800748.
114. Yoon S, Jo C, Noh SY, Lee CW, Song JH, Lee J. Development of a high-performance anode for lithium ion batteries using novel ordered mesoporous tungsten oxide materials with high electrical conductivity. Phys Chem Chem Phys. 2011;13:11060.
115. Gao L, Wang X, Xie Z, Song W, Wang L, Wu X, Qu F, Chen D, Shen G. High-performance energy-storage devices based on $WO_3$ nanowire arrays/carbon cloth integrated electrodes. J Mater Chem A. 2013;1:7167.
116. Yu MP, Sun HT, Sun X, Lu FY, Hu T, Wang GK, Qiu H, Lian J. 3D WO3 nanowires/graphene nanocomposite with improved reversible capacity and cyclic stability for lithium ion batteries. Mater Lett. 2013;108:29.
117. Zhang WH, Yue L, Zhang F, Zhang QF, Gui X, Guan RF, Hou GH, Xu N. One-step in situ synthesis of ultrathin tungsten oxide@carbon nanowire webs as an anode material for high performance. J Mater Chem A. 2015;3:6102.
118. Yue L, Tang JL, Li F, Xu N, Zhang F, Zhang QF, Guan RF, Hong J, Zhang WH. Enhanced reversible lithium storage in ultrathin $W_{18}O_{49}$ nanowires entwined Si composite anode. Mater Lett. 2017;187:118.
119. Wang SZ, Wang Y, Song YC, Jia XH, Yang J, Li Y, Liao JX, Song HJ. Immobilizing polysulfide via multiple active sites in $W_{18}O_{49}$ for Li-S batteries by oxygen vacancy engineering. Energy Stor Mater. 2021;43:422.
120. Yan NF, Cui HM, You SY, Shi JS, Weng YQ, Liu YW. Tungsten nitride nanotubes as sulfur host material for high performance Li-S batteries. Inorg Chem Commun. 2022;140: 109458.
121. Zhang WK, Lin C, Cong S, Hou JY, Bin L, Geng F, Jin J, Wu MH, Zhao ZG. $W_{18}O_{49}$ nanowire composites as novel barrier layers for Li-S batteries based on high loading of commercial micro-sized sulfur. RSC Adv. 2016;6:15234.
122. Bayeh AW, Kabtamu DM, Chang YC, Chen GC, Chen HY, Liu TR, Wondimu TH, Wang KC, Wang CH. Hydrogen-treated defect-rich $W_{18}O_{49}$ nanowire-modified graphite felt as high-performance electrode for vanadium redox flow battery. ACS Appl Energy Mater. 2019;2:2541.
123. Yan J, Wang Q, Wei T, Fan ZJ. Recent advances in design and fabrication of electrochemical supercapacitors with high energy densities. Adv Energy Mater. 2014;4:1300816.
124. Zhao ZY, Xia KQ, Hou Y, Zhang QH, Ye ZZ, Lu JG. Designing flexible, smart and self-sustainable supercapacitors for portable/wearable electronics: from conductive polymers. Chem Soc Rev. 2021;50:12702.
125. Feng QK, Zhong SL, Pei JY, Zhao Y, Zhang DL, Liu DF, Zhang YX, Dang ZM. Recent progress and future prospects on all-organic polymer dielectrics for storage capacitors. Chem Rev. 2022;122:3820.
126. Nagamuthu S, Zhang Y, Xu Y, Sun J, Zhang Y, Zaman FU, Denis DK, Hou L, Yuan C. Non-lithium-based metal ion capacitors: recent advances and perspectives. J Mater Chem A. 2022;10:357.
127. Simon P, Gogotsi Y. Materials for electrochemical capacitors. Nat Mater. 2008;7:845.
128. Park S, Shim HW, Lee CW, Song HJ, Kim JC, Kim DW. High-power and long-life supercapacitive performance of hierarchical, 3-D urchin-like $W_{18}O_{49}$ nanostructure electrodes. Nano Res. 2016;9:633.

129. Thalji MR, Ali GAM, Algarni H, Chong KF. $Al^{3+}$ ion intercalation pseudocapacitance study of $W_{18}O_{49}$ nanostructure. J Power Sources. 2019;438: 227028.
130. Jung J, Kim DH. $W_{18}O_{49}$ nanowires assembled on carbon felt for application to supercapacitors. Appl Surf Sci. 2018;433:750.
131. Huang X, Zhang ZG, Li H, Wang HX, Ma TL. In-situ growth of nanowire $WO_{2.72}$ on carbon cloth as a binder-free electrode for flexible asymmetric supercapacitors with high performance. J Energy Chem. 2019;29:58.
132. Li KR, Shao YL, Liu SY, Zhang QH, Wang HZ, Li YG, Kaner RB. Aluminum-ion-intercalation superapacitors with ultrahigh areal capacitance and highly enhanced cycling stability: power supply for flexible electrochromic devices. Small. 2017;13:1700380.
133. Thalji MR, Ali GAM, Liu P, Zhong YL, Chong KF. $W_{18}O_{49}$ nanowires-graphene nanocomposite for asymmetric supercapacitors employing AlCl3 aqueous electrolyte. Chem Eng J. 2021;409: 128216.
134. Tong ZQ, Tian YL, Zhang HM, Li XG, Ji JY, Qu HY, Li N, Zhao JP, Li Y. Recent advances in multifunctional electrochromic energy storage devices and photoelectrochromic devices. Sci Chin Chem. 2017;60:13.
135. Wang H, Yao CJ, Nie HJ, Yang L, Mei SL, Zhang QC. Recent progress in integrated functional electrochromic energy storage devices. J Mater Chem C. 2020;8:15507.
136. Li H, Firby CJ, Elezzabi AY. Rechargeable aqueous hybrid $Zn^{2+}$/$Al^{3+}$ electrochromic batteries. Joule. 2019;3:2268.
137. Li H, McRae L, Firby CJ, Elezzabi AY. Rechargeable aqueous electrochromic batteries utilizing Ti-substituted tungsten molybdenum oxide based $Zn^{2+}$ ion intercalation cathodes. Adv Mater. 2019;31:1807065.
138. Chen XL, Lin HJ, Deng J, Zhang Y, Sun XM, Chen PN, Fang X, Zhang ZT, Guan GZ, Peng HS. Electrochromic fiber-shaped supercapacitors. Adv Mater. 2014;26:8126.
139. Yuksel R, Coskun S, Gunbas G, Cirpan A, Toppare L, Unalan HE. Silver nanowire/conducting polymer nanocomposite electrochromic supercapacitor electrodes. J Electrochem Soc. 2017;164:A721.
140. Wang JQ, Liu J, Hu MM, Zeng J, Mu YB, Guo Y, Yu J, Ma X, Qiu YJ, Huang Y. A flexible, electrochromic, rechargeable Zn// PPy battery with a short circuit chromatic warning function. J Mater Chem A. 2018;6:11113.
141. Sun SB, Tang CG, Jiang YC, Wang DS, Chang XT, Lei YH, Wang NN, Zhu YQ. Flexible and rechargeable electrochromic aluminium-ion battery based on tungsten oxide film electrode. Sol Energy Mater Sol Cells. 2020;207: 110332.
142. Wang CC, Wang ZY, Ren YY, Hou X, Yan F. Flexible electrochromic Zn mirrors based on Zn/viologen hybrid batteries. ACS Sustainable Chem Eng. 2020;8:5050.
143. Zhong Y, Xia X, Mai W, Tu J, Fan H. Integration of energy harvesting and electrochemical storage devices. Adv Mater Technol. 2017;2:1700182.
144. Wu Z, Li XH, Qian AW, Yang JY, Zhang WK, Zhang J. Electrochromic energy-storage devices based on inorganic materials. Prog Chem. 2020;32:792.
145. Tian YY, Cong S, Su WM, Chen HY, Li QW, Geng FX, Zhao ZG. Synergy of $W_{18}O_{49}$ and polyaniline for smart supercapacitor electrode integrated with energy level indicating functionality. Nano Lett. 2014;14:2150.
146. Hassan M, Abbas G, Lu Y, Wang Z, Peng Z. A smart flexible supercapacitor enabled by a transparent electrochromic electrode composed of $W_{18}O_{49}$ nanowires/rGO composite films. J Mater Chem A. 2022;10:4870.
147. Li YT, Yan LT, Zhang L, Song XD, Dai CA. Design of electrochromic supercapacitor based on rGO-$W_{18}O_{49}$ nanowires/polyaniline. J Mater Sci-Mater El. 2021;32:19179.
148. Yan NF, Gao XP. Photo-assisted rechargeable metal batteries for energy conversion and storage. Energy Environ Mater. 2022;5:439.
149. Yan NF, Zhang WH, Cui HM, Feng XJ, Liu YW, Shi JS. Potassium phosphotungstate spheres as an anode material for a solar rechargeable battery. Sustain Energy Fuels. 2018;2:353.


**Publisher's Note** Springer Nature remains neutral with regard to jurisdictional claims in published maps and institutional affiliations.

Springer Nature or its licensor (e.g. a society or other partner) holds exclusive rights to this article under a publishing agreement with the author(s) or other rightsholder(s); author self-archiving of the accepted manuscript version of this article is solely governed by the terms of such publishing agreement and applicable law.